MATERIAL CHARACTERIZATION USING PASSIVE MULTISPECTRAL POLARIMETRIC IMAGERY

THESIS

Melissa A. Sawyer, Captain, USAF

AFIT-ENG-13-M-44

DEPARTMENT OF THE AIR FORCE
AIR UNIVERSITY

AIR FORCE INSTITUTE OF TECHNOLOGY

Wright-Patterson Air Force Base, Ohio

The views expressed in this thesis are those of the author and do not reflect the official policy or position of the United States Air Force, the Department of Defense, or the United States Government.

AFIT-ENG-13-M-44

MATERIAL CHARACTERIZATION USING PASSIVE MULTISPECTRAL POLARIMETRIC IMAGERY

THESIS

Presented to the Faculty

Department of Electrical and Computer Engineering

Graduate School of Engineering and Management

Air Force Institute of Technology

Air University

Air Education and Training Command

in Partial Fulfillment of the Requirements for the

Degree of Master of Science in Electrical Engineering

Melissa A. Sawyer, B.A., B.S.E.E., M.B.A

Captain, USAF

March 2013

AFIT-ENG-13-M-44

MATERIAL CHARACTERIZATION USING PASSIVE MULTISPECTRAL POLARIMETRIC IMAGERY

Melissa A. Sawyer, B.A., B.S.E.E., M.B.A
Capt, USAF

Approved:

Maj Milo W. Hyde, PhD (Chairman)	18 Mar 2013 Date
Col(s) Karl C. Walli, PhD (Member)	18 Mar 2013 Date
Lt Col James A. Louthain, PhD (Member)	13 Mar 2013 Date

AFIT-ENG-13-M-44

Abstract

A new method for characterization of unknown targets using passive multispectral polarimetric imagery is presented. Previous work makes use of a pBRDF derived equation for the degree of linear polarization and with the aid of measurements at multiple incident angles estimates refractive index and reflection angle. This work uses known incident and reflection angles along with dispersion equations and polarimetric data at multiple wavelengths to recover the index of refraction. Although imagery is collected with a division of time polarimeter and a spectral filter wheel in iterative, manual steps, the new algorithm could be applied to any set of registered multispectral polarimetric images most notably those produced by a recently introduced division of focal plane multispectral polarimetric sensor. Experimental results are presented showing the novel algorithm's ability to classify and characterize a range of materials.

To my father, whose work ethic and devotion to family are my life's aspirations.

Acknowledgements

I am forever indebted to my thesis advisor Maj Milo W. Hyde IV. His intellect, insight, and infallible patience were key to my successful completion of this research and it is not humanly possible to thank him enough. AFIT and the Air Force in general should be proud to have such an approachable, reasonable, and admirable leader among their ranks. I absolutely recognize how fortunate I was to have gotten the chance to work with Maj Hyde. Thank-you for everything Sir.

The support of my colleagues Mark Spencer, Mike Steinbock, and Steve Maksim helped me keep some semblance of sanity and their dedication provided me the motivation to double-down on my efforts to do well at AFIT.

The Institute itself deserves many thanks. The opportunity to devote oneself fully to classes and research is rare in a Master's program and AFIT provides that opportunity to hundreds of students each year. I feel as if I truly matured at AFIT, both as an officer and as a person. The coursework pushed my mental limits and the research taught me how to teach myself, a lifelong skill for which I will forever be grateful. I know I am a stronger person for having put forth the dedication and focus necessary to do well at AFIT and without the rigorous coursework and stellar military and civilian faculty that would not have been possible.

Lastly, and most importantly, I could not have gotten through AFIT without the love and support of my husband Nick Olson. He kept the house running, put up with my crazy hours, and was always there when I needed a shoulder to lean on. Nick's willingness and ability to communicate and work through all the new stressors this assignment imposed on our relationship amazes me every day and makes me so proud to call him my husband.

Melissa A. Sawyer

Table of Contents

Page

List of Figures

List of Tables

List of Acronyms

Acronym	Definition
Al	Aluminum
AOP	Angle of Polarization
ATS	Atmospheric Turbulence Simulator
BRDF	Bidirectional Reflectance Distribution Function
DOP	Degree of Polarization
DOLP	Degree of Linear Polarization
EM	Electromagnetic
FOV	Field of View
GPS	Global Positioning System
IR	Infrared
LED	Light Emitting Diode
LiDAR	Light Detection and Ranging
MATLAB	Matrix Laboratory
MS	Multispectral
MSSI	Multispectral Stokes Imager
MTF	Modulation Transfer Function
NASA	National Aeronautics and Space Administration
OPTECS	Optical Turbulence Estimation, Compensation, and Simulation
OTF	Optical Transfer Function
pBRDF	Polarimetric Bidirectional Reflectance Distribution Function
PI	Polarimetric Imaging
PSF	Point Spread Function
RADAR	Radio Detection and Ranging

Acronym	Definition
RGB	Red, Green, and Blue 37
RS	Remote Sensing 2
SAR	Synthetic Aperture Radar 8
SONAR	Sound Navigation and Ranging 8
TEM	Transverse Electromagnetic 1
UV	Ultraviolet 18

MATERIAL CHARACTERIZATION USING PASSIVE MULTISPECTRAL POLARIMETRIC IMAGERY

I. Introduction

Optics, the study of light and its interaction with matter, has a rich history dating back to the first use of mirrors many centuries before the common era [12] and obligates the mention of great scientists and mathematicians such as Snell, Fermat, Huygens, Newton, Faraday, Maxwell, Planck, and Einstein [16]. The theories, experiments, and equations generated by these great minds (and many others) allow our modern understanding of light's duality; its existence as quantized particles called photons and as waves. Of particular interest to this research is the propagation of light shown by Maxwell's equations to take the form of a Transverse Electromagnetic (TEM) wave.

Polarization (discussed further and graphically illustrated in Chapter II) is defined as the orientation of the electric field vector of a TEM wave with respect to its propagation axis. The polarization state of light, although imperceivable to the human eye, can be mathematically derived and used to determine valuable information about the object from which the light is scattered. The goal of this research is to use polarization data at multiple wavelengths in a novel way such that an unknown object's index of refraction is recovered.

Over the past three decades efforts have increased to "fuse" data from sensors of differing modalities (Multispectral (MS), thermal, etc.) to more accurately identify targets of interest [50]. Advances in nanofabrication now allow construction of a unified MS polarimetric sensor on one substrate [19], eliminating the need to fuse data from separate MS and Polarimetric Imaging (PI) sensors. The algorithm developed in this work could exploit the data generated by this new sensor to more accurately detect high value targets.

1.1 Problem Statement and Hypothesis

The refractive index of a solid material is a measure of the speed at which light travels through that material relative to the speed of light in a vacuum and is dependent upon the incident light's wavelength. Depending on the Remote Sensing (RS) technique employed, recovering an object's index of refraction may require the determination of a large set of unknown and often coupled parameters. With regards to polarimetric RS there exists an equation (given and further defined in Chapter II) that expresses the Degree of Polarization (DOP) of light scattered from an object as a function of the object's refractive index and the light's angles of incidence and reflection [18,29,34,37,42]. Thilak *et al.* used this equation to estimate an object's complex refractive index and the angle of reflection by acquiring multiple images, each with a different angle of incidence [42]. This research seeks an answer to the following problem statement: could an estimate be made of a target's index of refraction with a single MS polarimetric image?

It is reasonable to assume the Sun's and a remote sensing platform's zenith angle with respect to a target (θ_i and θ_r respectively in Fig. 1) are known via Global Positioning System (GPS) and inertial measurement unit ephemeris data and a data collection time stamp. Therefore, a novel hypothesis is formed that with known θ_i and θ_r angles and DOP measurements collected simultaneously at multiple wavelengths, the target's index of refraction can be estimated via a non-linear least squares fit using two dispersion equations.

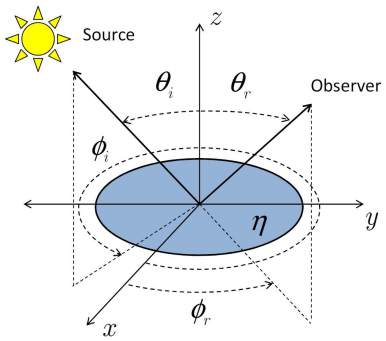

Figure 1: Viewing Geometry [18]

1.2 Scope and Assumptions

In order to remotely recover one of a target's many potential physical properties such as its refractive index, a method must be found to isolate that parameter in a set of equations such that solving for the parameter of interest is feasible. To simplify this multi-dimensional problem assumptions are frequently made about the target's environment, its other physical properties, and the RS viewing geometry. The assumptions necessary to ensure successful completion of this work, thus limiting its scope, are detailed below. Many of these assumptions align with those made by Hyde [18].

The first two assumptions impose limitations on the target's environment. The illumination source is assumed to be passive and unpolarized (or randomly polarized) and the target is expected to be stationary with respect to its environment. In an operational environment the first assumption simply means the Sun is expected to be the light source. This condition allows for a common reduction in scope related to calculating the polarimetric state of the light scattered off the target as described in sections 2.2.3 and 2.3.3. A stationary target is important as pixel misregistration can cause misclassification and/or mischaracterization of the target. Two components of this work's experimental instrument, a manual spectral filter wheel and a focusing lens in front of the camera, have the potential to contribute to pixel registration issues. Part of this work's data analysis algorithm includes averaging experimental values on a pixel-by-pixel basis across measurements made at different wavelengths, so any change in image alignment due to rotation of the filter wheel or defocus due to chromatic aberration apparent on the camera's focal plane between measurements could cause pixel misclassification and/or mischaracterization. The method used to mitigate this issue is described in sections 3.1.3 and 4.2.

The third, fourth, and fifth assumptions limit the physical properties of the targets of interest (dielectrics and metals). All targets are assumed to be non-magnetic, of room temperature (300K), and isotropic. The refractive index of a material η is defined by its

intrinsic properties: permeability, conductance, and permittivity [18, 28]. Any changes to these properties must be accounted for in assumptions regarding their applicability to this work or by the functional form used for refractive index. The materials examined in this work do not have a magnetic response at optical frequencies, therefore their permeability is assumed to not be of concern. Changing conductance does not apply to dielectrics since by definition dielectrics are non-conductive. The conductance of metals changes as a function of temperature which is accounted for in the damping term of the Drude model-derived functional form of the refractive index (see Eq. (3)) [16]. A material's permittivity (its susceptibility to dipole moment polarization upon interaction with an external electric field) relative to that of free space is its relative permittivity. Given the assumptions already made here, the index of refraction is defined as simply the square root of a medium's relative permittivity. The results of this work display changes in relative permittivity over wavelength and an assumption regarding temperature is made to account for changes in permittivity due to temperature. Most available refractive index values are experimentally found at room temperature [28] and the targets of interest exclude those of high temperature such as engine exhaust, so the assumed temperature of 300K is reasonable and allows for comparison of this work's results to those available in the literature. In general, permittivity changes over the surface of a material, but even at visible wavelengths the contributions of a large number of atoms are averaged during imaging and represent the behavior of an isotropic dielectric [16]. Assuming isotropy allows for the reduction of the generic dielectric tensor to a scalar, greatly simplifying the mathematical framework necessary for finding the index of refraction.

The final two assumptions limit the viewing geometry and imaging instrument conditions. All imaging is assumed to occur in the specular plane without any pixel saturation. The specular plane is defined as that containing the target's surface normal vector and the incident and reflected light's propagation direction vectors. The

experimental instrument used in this work is currently set up for data collection in only the specular plane. Extension to out-of-plane measurements is left to future work. Pixel saturation causes inaccuracy of the calculated polarimetric data and leads to pixel misclassification and/or mischaracterization, so care was taken to ensure no pixel saturation during the acquisition of irradiance data. Implementation of this algorithm should be limited to systems that either have a variable source intensity or a camera with a high enough dynamic range to ensure no or very little pixel saturation.

1.3 Thesis Overview

An introduction to the problem addressed by this research, the author's proposed answer to that problem, and assumptions necessary to simplify the problem were presented in Chapter I. Chapter II steps through the academic and mathematical background necessary to understanding the author's approach to proving the given hypothesis. Chapter III shows how, given the background developed in Chapter II, the author arrived at the stated hypothesis and how that hypothesis was tested via experimentation. Experimental results and analyses thereof are given in Chapter IV while Chapter V offers concluding remarks and potential future extensions to this work.

II. Background and Related Research

An attempt is made in this chapter to ease the reader into the presented research by starting with a broad concept and continually narrowing the topic focus until the specific mathematical framework used in this work is presented at the end. An overview is given of conventional remote sensing approaches and the case is made for the specific concept of combining multispectral and polarimetric remote sensing. The scope is then focused further by providing the theory underlying each term of this work's title. Finally, the chapter delves into the mathematical framework developed in related research and leveraged in this work.

2.1 Remote Sensing

The term remote sensing is attributed to any effort to obtain information about an object without physically coming into contact with said object. A few of the many possible examples of remote sensing include gathering information about the cosmos with a telescope, mapping Earth's weather patterns using a satellite, or measuring the speed of a moving vehicle with a radar gun. Each of these examples involves the detection and measurement of Electromagnetic (EM) radiation of different wavelengths reflected or emitted from the object(s) of interest. The specific wavelength boundaries of each named region of the EM spectrum vary depending on the source consulted with one such interpretation offered in Fig. 2 [38].

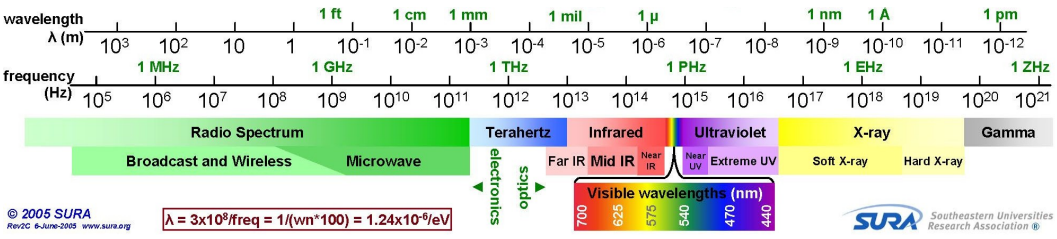

Figure 2: Electromagnetic Spectrum [38]

Remote sensing of EM energy can occur in a lab setting, but most often RS refers to gathering information about a distant object from Earth's surface or information about Earth from an aerial or space asset. In order to detect radiation of a particular wavelength, a system's sensor must be designed such that it is sensitive to that wavelength and can "see" that wavelength through Earth's atmosphere. Energy from the Sun in the form of mainly Infrared (IR) and visible light impinges on Earth's atmosphere (Fig. 3a) where it is absorbed or transmitted according to Fig. 3b [21]. The wavelengths at which energy is blocked correspond to specific atmospheric molecules that absorb that wavelength of incoming radiation. Acquiring RS data is limited to the non-blocked spectral regions, the "atmospheric windows." Figure 3c shows which RS systems are useful in each atmospheric window region. The next section gives a cursory explanation and examples of but a few conventional RS systems [21].

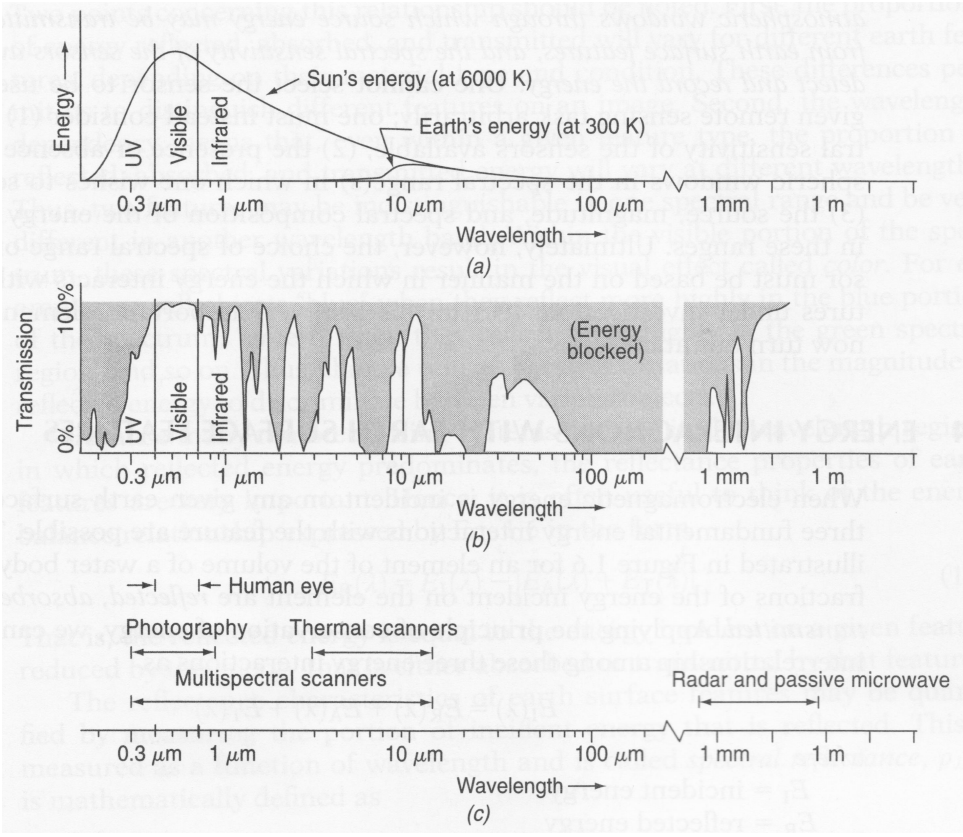

Figure 3: Spectral Characteristics of (a) the Sun and Earth, (b) Atmospheric Transmittance, and (c) Common Remote Sensing Systems [21]

2.1.1 Conventional Approaches.

As shown by Fig. 3c, RS systems can be classified by the wavelength region they operate over, but of greater interest to this work is the classification of a RS system as active or passive. Active systems produce a signal of a particular EM energy, send that signal towards an object or scene of interest, and then use the measurement of the returned signal to make observations about the object. Passive systems detect naturally occurring EM energy, such as that from the Sun, scattered and/or emitted from an object.

Examples of active remote sensing systems include Radio Detection and Ranging (RADAR), Light Detection and Ranging (LiDAR), and Sound Navigation and Ranging (SONAR). RADAR systems transmit radio frequency EM waves, often times with a specifically generated polarization state, toward a region of interest and receive and detect these EM waves when reflected from objects in that region. Among many other applications, RADAR is used for detection and tracking of targets of interest, creating two and three dimensional maps, collision avoidance, and Earth resources monitoring [31]. RADAR's advantages include all-weather performance, day and night capability, and an ability to penetrate a modest depth into the surface of the Earth. The biggest disadvantage of RADAR is a system's resolution (its ability to discern between two closely spaced objects) is limited by its antenna size and wavelength. A technique called Synthetic Aperture Radar (SAR) is used to overcome this limitation, but for the sake of brevity will not be covered here. An example of a RADAR product collected over two radio wavelengths with multiple polarization states displayed in false colors is shown in Fig. 4a [32].

LiDAR systems emit laser light in the near IR and visible portions of the EM spectrum and measure the time it takes for the sensor to detect the reflected light. The laser light is emitted from the system in rapid succession to form a "point cloud" of raw LiDAR data in which each point represents a three dimensional coordinate with respect to the known sensor location. Return intensity, number of multiple returns (when the light reflects off

more than one object before returning to the sensor), and scan angle information is also encoded as part of each data point. Some applications of LiDAR include water depth analysis, terrain mapping, and tree canopy profiling [25]. One distinct advantage of LiDAR is its raw data is georeferenced from inception, simplifying image production [21]. Calibrating the sensor's location to produce the georeferenced raw data, however, can be a tedious process since a surveyed ground-based GPS location near the survey area is necessary. An example of a LiDAR product is shown in the upper portion of Fig. 4b showing the "bare ground" elevation of Mount Hood in Oregon [27].

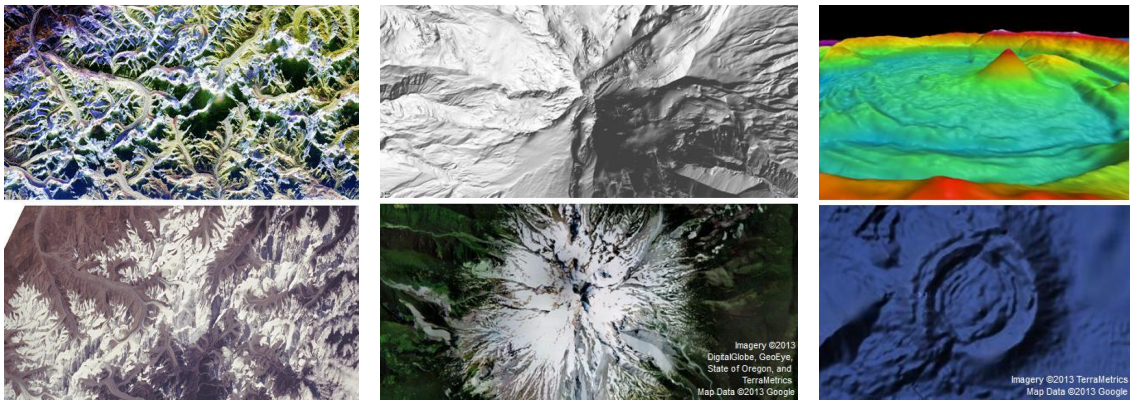

(a) RADAR - Mount Everest [32] **(b) LiDAR - Mount Hood [27]** **(c) SONAR - Lau Basin [23]**

Figure 4: Active Remote Sensing Product Examples and Their Optical Counterparts

SONAR systems rely on mechanical acoustic waves for navigation and object detection purposes rather than on the EM waves used by other RS systems. Sound waves travel longitudinally (versus transversely) in most mediums via compression and rarefaction of the medium ahead of the wave in the direction of propagation. The sound wave pulses created by a SONAR system's transducer reflect off objects of differing mediums and that reflected echo is received by the system. High frequency SONAR is used for mapping sea floors, medium frequency military systems detect submarines and underwater objects, and low frequency systems detect large objects over further

distances [24]. An example of SONAR imagery is Fig. 4c which shows the caldera of an underwater volcano in the Lau Basin near the Samoan Islands [23]. The bottom portion of Fig. 4c is imagery available via the Google Maps™ mapping service and is a combination of SONAR data and satellite altimetry, a RADAR technique. SONAR can also be an example of a passive RS system when used in "listen" mode only; detecting naturally occurring sounds rather than the reflection of artificially generated sound waves [20].

More common passive RS techniques include thermal, panchromatic, multispectral, and polarimetric imaging. Thermal detectors such as thermocouples and bolometers sense emitted IR radiation. Any minute change in temperature triggers a change to the resistivity in the detector's circuitry in the case of a bolometer and a change in the voltage across two dissimilar metal leads in the case of a thermocouple [51]. These changes in resistivity or voltage can be processed into an image such as that shown in Fig. 5a displaying energy loss through a window header [41]. Thermal imaging applications include detection of energy radiated from water vapor at the top of the atmosphere revealing weather patterns, military technology such as night vision goggles, and satellites that can detect the launch of ballistic missiles. The main advantage of thermal imaging is its day and night capability, but one shortcoming is the slow response time of most thermal detectors compared to photodetectors.

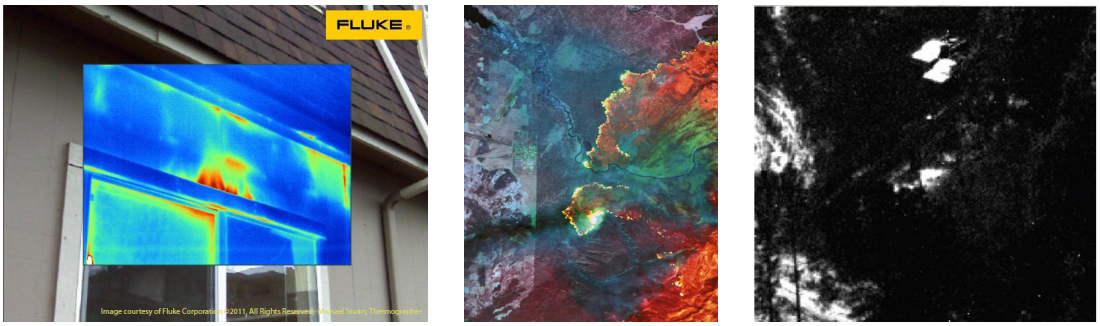

(a) Thermal [41] **(b) Multispectral [9]** **(c) Polarimetric [47]**

Figure 5: Passive Remote Sensing Product Examples

Surrounding the thermal image in the center of Fig. 5a is a panchromatic image. Panchromatic (or grayscale) images are formed by electronically converting the number of photons incident onto a detector over a broad wavelength spectrum, usually in the visible band, into a value representing the radiance of the scene of interest. This type of image only conveys information about the apparent brightness of the scene and is unable to convey color information. Visible multispectral imagery is the process of taking panchromatic images over multiple narrow wavelength bands of interest. Each spectral image appears as grayscale until processing techniques are used to combine the images into a "true" or "false" color image. The most common mutispectral bands are red, green, and blue which are combined to produce a true color image showing a scene as it might look to the human eye. Figure 5b shows a false color multispectral image of the 1988 Yellowstone fires taken by a twelve band imager aboard a National Aeronautics and Space Administration (NASA) owned aircraft helping authorities track the fire's progression through the park [6, 8, 9].

2.1.2 Passive Multispectral Polarimetric Remote Sensing.

The least intuitive RS technique is undoubtedly polarimetry. Polarization is a property of all TEM waves, so its applications are not limited to any specific wavelength region. Most RS textbooks only discuss polarization with regards to its application in RADAR systems, including a text solely committed to the topic of applications of polarization in remote sensing [5, 21, 26]. A recent text by Schott [36] recognizes that "lack of data continues to prevent many application scientists from evaluating the value of PI remote sensing... it is the need for better understanding by the potential user community of the subtleties of PI that prompted the development and structuring of this text." Passive PI's utility lies in the fact that when natural (unpolarized) light scatters off a natural or man-made object its polarization state is altered. Figure 5c is a polarimetric image of an outdoor scene containing a thick line of trees, a grassy area, and two pickup trucks parked in the shade under the trees. The interested reader is referred to Tyo's [47] Fig. 1 for true color and

long-wave IR intensity representations of the scene. As shown in Tyo's work, the trucks are not visible in the true color or the long-wave IR intensity images. The polarimetric image, however, distinctly reveals the vehicles in the upper middle portion of the image. As shown in this work, PI can unearth more than simply the presence of man-made targets. If MS functionality is added to a polarimetric imager, this work's proposed algorithm could recover the target's refractive index, thus determining its surface material. Even in the absence of polarization content (which is typical at near-normal incidence) the true color images produced by a MS polarimetric imager would still be useful for target identification.

2.2 Title Components Theory

With the immense diversity of possible RS techniques established and the case made for combining multispectral and polarimetric RS, the focus of Chapter II is narrowed to detailing the theory behind each component of this work's title.

2.2.1 Material Characterization.

As introduced in section 1.2, the permittivity, conductance, and permeability of a material are conveyed by its index of refraction. Characterizing a material involves finding a physical theory linking the refractive index to measurable parameters of interest allowing for either direct inversion to recover the refractive index or solving via least squares methods. In this work the index of refraction is found using Matrix Laboratory (MATLAB)'s *lsqcurvefit* function, a non-linear data-fitting least squares solving method. In order for *lsqcurvefit* to recover a material's refractive index, the material must first be classified. Classifying a material as either dielectric or metallic is less complicated than full characterization in that precisely solving for the refractive index is not necessary. Given an empirical data set, a researcher can decide on some threshold criteria with which to classify the material. Full characterization via RS is desirable for intelligence gathering, non-destructive inspection, and many other situations when physical contact with a material is denied or unsuitable.

2.2.2 Multispectral.

Having defined multispectral imagery in section 2.1.1, this section focuses on one complication applicable to this work that arises when taking multiple narrow band images of a scene: chromatic aberration. Figure 6 shows dispersion (discussed further in section 2.3.2) of incident light rays causing the focal point of each wavelength to differ [30]. The optical components of this work's experimental setup were installed to optimize performance at the 633nm focal point, thus imaging any other wavelength produces a defocused image. Without a complete system redesign, this problem could have been remedied by finding the system's Point Spread Function (PSF) at each wavelength and deconvolving each defocused image, but a simpler approach (manual focusing) was used in the interest of time.

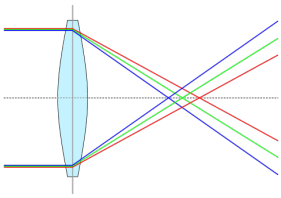

Figure 6: Chromatic Aberration Caused by a Convex Lens [30]

2.2.3 Polarimetric.

Figure 7 depicts how EM (light) waves propagate; the electric field is perpendicular to the magnetic field and both are perpendicular to the direction of propagation ($\mathcal{E}$, $\mathcal{H}$, and z in the figure, respectively). The polarimetric state of the wave shown in Fig. 7 is considered linear and vertical since the projection of the electric field vector as it propagates traces out a vertical line in the xy plane. The wave in Fig. 8a is also considered linear, but is oriented at 45° with respect to the x axis as shown by the dotted trace of its $\mathcal{E}_x$ and $\mathcal{E}_y$ components onto the xy plane [36]. Figure 8 also shows how a TEM wave's polarization state may be circular or elliptical and can appear to rotate counterclockwise as in Fig. 8b or clockwise as in Fig. 8c [36]. Although not perfectly so, sunlight is considered unpolarized meaning the electric field is randomly oriented as the wave propagates.

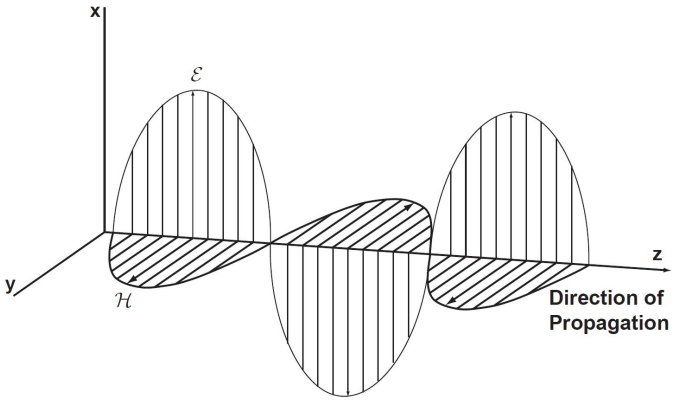

Figure 7: Fluctuations in the Electric and Magnetic Fields Give Rise to TEM Wave Propagation in the z Direction [36]

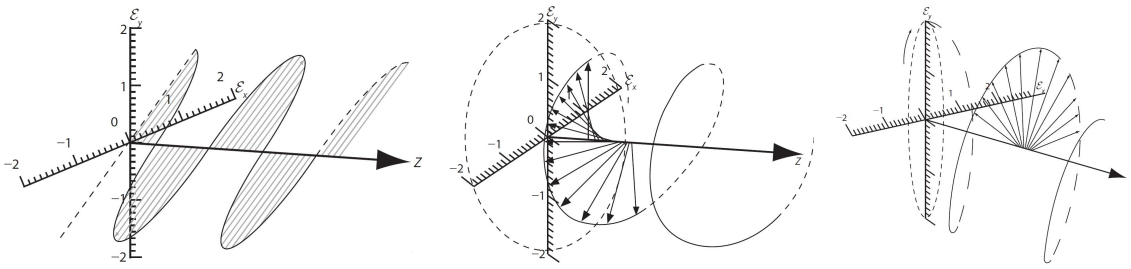

(a) Linear **(b) Circular** **(c) Elliptical**

Figure 8: Polarization States [36]

Polarization state cannot be measured by any sensor directly, but can be calculated from the electric field's irradiance. Introduced by G. G. Stokes in 1852, Stokes parameters are used to represent light's polarization state [16]. An interpretation of how the parameters characterize polarization state is offered in Table 1 [36]. Conventionally, each Stokes parameter is normalized to the S_0 value, allowing better representation of how much each parameter contributes to the wave's polarimetric state.

Table 1: Meaning of Stokes Parameter Values, Modified from Schott [36]

Parameter	Positive	Negative
S_0	Represents total $\mathcal{E}$ field irradiance	N/A
S_1	Horizontal polarization dominates	Vertical polarization dominates
S_2	+45° polarization dominates	−45° polarization dominates
S_3	Right-hand circular dominates	Left-hand circular dominates

The last Stokes parameter, S_3, is not applicable to this work. When illuminated by a natural source, light scattered from an object has been shown to contain an insignificant amount of circularly polarized light [7,18,22,37,49]. As a consequence of this observation, the polarization analyzer used by this work need only consist of a linear polarizer. The mathematical implication of this simplification is explained in section 2.3.3.

2.2.4 Imagery.

In the context of this research, images are a series of grayscale irradiance measurements collected of an unknown target using a multispectral polarimeter. The system required calibration and characterization before any experimental data was collected. If the system was ideal, its resolution would be limited only by diffraction caused by its entrance pupil, a circle. The diffraction pattern measured when imaging a point source is the system's PSF. In the frequency domain, the inverse Fourier transform of the PSF is the system's Optical Transfer Function (OTF) and conveys which frequencies are attenuated or passed by the system. The Modulation Transfer Function (MTF) is the absolute value of the OTF and is typically normalized and plotted as a function of cutoff frequency. One way to measure the quality of an imaging system, thus aiding in calibration, is to determine its MTF. Any operational optical system will suffer from aberrations (defocus, spherical, etc.) that degrade image quality. The aberrations are apparent in the system's MTF. A set of orthogonal polynomials called Zernikes can be used to determine how many waves of each aberration exist in a system. Each aberration's polynomial is added together and applied as a phase to a complex pupil function. The pupil function is then Fourier transformed to obtain the amplitude spread function. The absolute value of the amplitude spread function gives the PSF, and then as before, the MTF is found. The mathematical form of diffraction limited MTF curves are known and are plotted along with a system's MTF to show how near an imaging system is to diffraction limited performance. Data showing the performance of the instrument used in this work is given in section 3.1.2.

2.3 Mathematical Framework

With the theoretical context of this work defined, this section presents the specific mathematical framework used to produce this work's results.

2.3.1 Complex Index of Refraction.

A material's complex index of refraction $\eta = n - \mathrm{j}k$ is a combination of two optical constants: index of refraction n and extinction coefficient k. The refractive index n is defined as the ratio of phase velocity of light in vacuum to the phase velocity of light in the medium ($n = c/v$). The extinction coefficient k is related to the exponential decay of the wave as it passes through the medium [2] and can be thought of as representing absorption.

2.3.2 Dispersion Equations.

Since the underlying physical parameters that define the refractive index (conductivity, permeability, and permittivity) depend on wavelength, so does η itself. Dispersion refers to the phenomena whereby a medium's index of refraction is frequency (wavelength) dependent [16]. Evidence of dispersion is shown by shining a light containing all visible wavelengths (a white light) onto a prism as seen in Fig. 9 [10]. A material's refractive index is measured over many wavelengths to produce its dispersion curve such as that for gold in Fig. 10 [28].

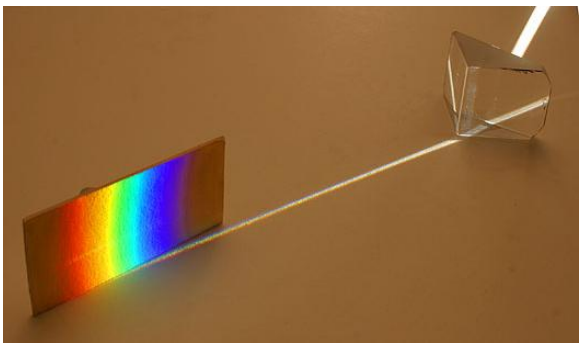

Figure 9: Dispersion of White Light Through a Prism [10]

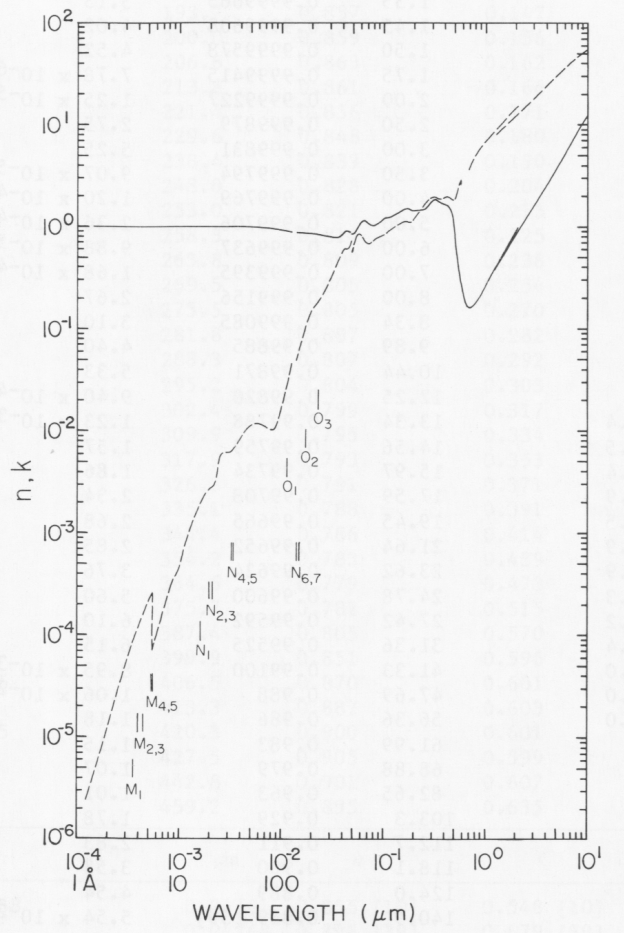

Figure 10: Empirical Dispersion Curve of Gold, *n*(-), *k*(- -) [28]

Empirical dispersion curves are available for a wide variety of materials and are approximated by dispersion equations such as the Cauchy equation:

$$n(\lambda) = A_0 + \sum_{i=1} \frac{A_i}{\lambda^2} \tag{1}$$

the Sellmeier equation:

$$\eta^2(\lambda) = 1 + \sum_{i=1} \frac{A_i \cdot \lambda^2}{\lambda^2 - C_i^2} \tag{2}$$

and the Drude model:

$$\eta^2(\omega) = 1 - \left(\frac{\omega_p^2}{\omega^2 + \mathrm{j}\omega\tau^{-1}} \right) \tag{3}$$

where $\omega = 2\pi c/\lambda$, ω_p is plasma frequency, and τ is electron relaxation rate [13, 16].

The constants A_0, A_i, and C_i in Eq. (1) and Eq. (2) are borne out of what's happening to a dielectric at the atomic level as it's bombarded by a harmonic EM wave. The Lorentz model of light/matter interaction likens the bonds between electrons and their nuclei to the classical mechanics concept of a small mass connected by a spring to a larger mass. An incident electric field induces displacement of the electrons which then undergo a spring-like restoring force toward equilibrium. The natural resonance frequencies in a volume of molecules due to these spring-like oscillations give rise to multiple oscillatory modes. The dispersion equation constants give the wavelength at which those modes occur and the relative strength of each mode. The interested reader is referred to Hecht [16] section 3.5.1 for more detail. Although the Lorentz model was not published until the late 1890s, Cauchy published his equation for dispersion in 1835 based on his own theory (or arguably Fresnel's theory) of how particles responded to an external force [3]. Sellmeier's equation better predicts dispersion over a wider wavelength range and was published in 1871 [2]. Since this work is limited to the visible portion of the EM spectrum, the Cauchy equation is sufficient for estimating the refractive index of dielectrics.

As mentioned above, the Lorentz model treats electrons as bound to the nucleus by a harmonic restoring force thus representing a non-conductive dielectric. The Drude model is identical to the Lorentz model, but sets the restoring force to zero thus allowing the electrons to move freely representing a metal [2]. Free electrons and positive ions within a metal may be thought of as a plasma whose density oscillates at a natural frequency ω_p, the plasma frequency, which for most metals occurs within the visible or Ultraviolet (UV) bands [16]. As a consequence of the Drude model, the refractive index of metals is found using Eq. (3). This work's application of dispersion equations is explained in section 3.2.1.

Every material has wavelength bands within their dispersion curve that follow what are called "normal" and "anomalous" dispersion. *Normal* dispersion describes a band over which the real part of the refractive index *decreases* with *increasing* wavelength, whereas

anomalous dispersion occurs when *n increases* with wavelength [16]. Where these regions occur within the EM spectrum depend on where strong absorption occurs for that material. Absorption occurs when the incident light has a high enough energy to excite electrons within the material from a lower energy state to a higher energy state, thus "absorbing" the incoming energy. Most metals experience no absorption within the visible band and instead absorb in the UV region, meaning they undergo anomalous dispersion in the visible and reflect almost all visible light. As shown in Fig. 11 [17], the combination of the three additive colors red, green, and blue give most metals a white or silver appearance. Gold and copper are examples of metals that experience absorption in the visible band. Gold absorbs incident blue light, thus explaining how the remaining visible light that either reflects off of or is re-emitted by gold (red plus green) gives the material its yellow appearance. This also means gold experiences normal dispersion in the visible band. As a consequence of this information and the fact that this work's data is collected in the visible band, it is expected that upon evaluation of the metallic samples used in this work (gold and aluminum), gold's refractive index values will decrease with wavelength while aluminum's *n* values will increase with wavelength.

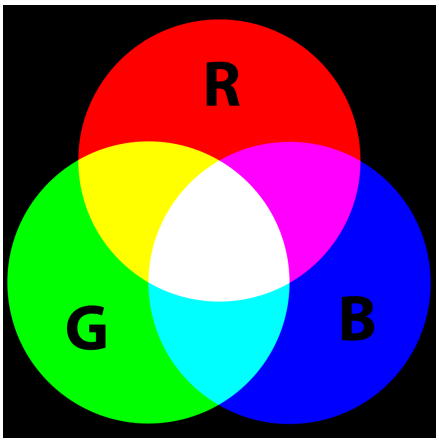

Figure 11: RGB Model of Additive Light [17]

2.3.3 Stokes Vectors and Mueller Calculus.

The meaning of each Stokes parameter was given in section 2.2.3. Using the axes convention given in Fig. 8 it is clear at any given time t the electric field vector $\vec{\mathcal{E}}$ has amplitude components $\mathcal{E}_{0x}$ and $\mathcal{E}_{0y}$ in the x and y planes, respectively. Together these components form a transverse harmonic plane wave such as that expressed by

$$\begin{aligned} \vec{\mathcal{E}} &= \vec{\mathcal{E}}_x(z,t) + \vec{\mathcal{E}}_y(z,t) \\ \vec{\mathcal{E}}_x(z,t) &= \mathcal{E}_{0x}\cos(kz - \omega t)\,\hat{\mathbf{i}} \\ \vec{\mathcal{E}}_y(z,t) &= \mathcal{E}_{0y}\cos(kz - \omega t + \epsilon)\,\hat{\mathbf{j}} \end{aligned} \tag{4}$$

where z is the position of the wave, ϵ is the relative phase difference between the wave's components (for linear polarization $\epsilon = 0,\ \pi,$ or 2π), k is the wavenumber (not to be confused with the extinction coefficient), and ω is the wave's angular frequency. The most general state of polarization is elliptical with linear and circular polarization being special cases thereof. In a derivation shown by Hecht [16], the time and position dependencies can be removed from Eq. (4) to express the electric field vector's projected ellipse on the xy plane given by

$$\left(\frac{\mathcal{E}_y}{\mathcal{E}_{0y}}\right)^2 + \left(\frac{\mathcal{E}_x}{\mathcal{E}_{0x}}\right)^2 - 2\left(\frac{\mathcal{E}_x}{\mathcal{E}_{0x}}\right)\left(\frac{\mathcal{E}_y}{\mathcal{E}_{0y}}\right)\cos\epsilon = \sin^2\epsilon \tag{5}$$

After some algebraic manipulation including time averaging as Schott mentions is shown in Stokes [36, 39], the projected ellipse can be expressed in the form

$$(\mathcal{E}_{0x}^2 + \mathcal{E}_{0y}^2)^2 = (\mathcal{E}_{0x}^2 - \mathcal{E}_{0y}^2)^2 + (2\mathcal{E}_{0x}^2\mathcal{E}_{0y}^2\cos\epsilon)^2 + (2\mathcal{E}_{0x}\mathcal{E}_{0y}\sin\epsilon)^2 \tag{6}$$

The Stokes parameters for a plane wave are thus defined in Schott [36] as

$$\begin{aligned} S_0 &= \mathcal{E}_{0x}^2 + \mathcal{E}_{0y}^2 \\ S_1 &= \mathcal{E}_{0x}^2 - \mathcal{E}_{0y}^2 \\ S_2 &= 2\mathcal{E}_{0x}^2\mathcal{E}_{0y}^2\cos\epsilon \\ S_3 &= 2\mathcal{E}_{0x}\mathcal{E}_{0y}\sin\epsilon \end{aligned} \tag{7}$$

The parameters depend only on measurable irradiances and are conventionally combined into a Stokes vector as

$$\boldsymbol{S} = [S_0 \quad S_1 \quad S_2]^{\mathrm{T}} \tag{8}$$

The Stokes vector given in Eq. (8) contains only S_0 through S_2 because, as explained in section 2.2.3, this work is only concerned with linearly polarized light and S_3 represents the amount of circularly polarized light. Examples of Stokes vectors representing commonly produced linear polarimetric states include

$$\begin{array}{llll} [1 \quad 0 \quad 0]^{\mathrm{T}} & \text{Unpolarized} & [1 \quad 1 \quad 0]^{\mathrm{T}} & \text{Horizontal} \\ [1 \quad -1 \quad 0]^{\mathrm{T}} & \text{Vertical} & [1 \quad 0 \quad 1]^{\mathrm{T}} & \text{Linear } 45^\circ \end{array} \tag{9}$$

which agree with the information presented in Table 1. The Degree of Linear Polarization (DOLP) is the degree to which light is linearly polarized (a value from 0 representing no linear polarization to 1 meaning light is fully linearly polarized) and is expressed in terms of the Stokes parameters as

$$\mathrm{DOLP} = \frac{\sqrt{S_1^2 + S_2^2}}{S_0} \tag{10}$$

The Angle of Polarization (AOP) is the angle the electric field vector makes with respect to the x axis and is defined in terms of Stokes parameters as

$$\mathrm{AOP} = \frac{1}{2} \arctan\left(\frac{S_2}{S_1}\right) \tag{11}$$

The goal of passive PI is to calculate an "input" Stokes vector $\boldsymbol{S}_{\mathrm{in}}$ which gives the polarization state of light scattered off a target of interest. The standard equation used to calculate $\boldsymbol{S}_{\mathrm{in}}$ is

$$\boldsymbol{S}_{\mathrm{out}} = \boldsymbol{M}_{\mathrm{sys}} \cdot \boldsymbol{S}_{\mathrm{in}} \tag{12}$$

where the S_0 parameter of the "output" Stokes vector $\boldsymbol{S}_{\mathrm{out}}$ is the total irradiance measured by the PI system ($\mathcal{E}_{0x}^2 + \mathcal{E}_{0y}^2$) and $\boldsymbol{M}_{\mathrm{sys}}$ is the PI system's Mueller matrix. Mueller matrices characterize the diattenuation and retardance of polarization elements and are known for

many optical components [2]. Any component of a PI system that may affect $\boldsymbol{S}_{\text{in}}$ before it reaches the imager such as a polarizer or retarder must be accounted for in the system Mueller matrix. If a system has more than one polarization altering component, each component's individual Mueller matrix can be multiplied to form one overall system Mueller matrix. Further discussed in section 3.1.2, calculation of $\boldsymbol{S}_{\text{in}}$ is straightforward with multiple measurements of S_0^{out} and a known $\boldsymbol{M}_{\text{sys}}$.

2.3.4 Fresnel Reflectance.

The equations governing how light interacts with matter are a good place to start when searching for a physical model relating the measurable Stokes parameter S_{out}^0 to the refractive index. Using Maxwell's equations, the law of reflection, and Snell's law of refraction, it can be shown [18] that the Fresnel reflection coefficients given by

$$\begin{aligned} R_s &= \left[\frac{(\cos\theta_i - A)^2 + B^2}{(\cos\theta_i + A)^2 + B^2}\right] \\ R_p &= \left[\frac{(A - \sin\theta_i \tan\theta_i)^2 + B^2}{(A + \sin\theta_i \tan\theta_i)^2 + B^2}\right] R_s \\ A &= \sqrt{\frac{\sqrt{C} + D}{2}} \qquad B = \sqrt{\frac{\sqrt{C} - D}{2}} \\ C &= 4n^2k^2 + D^2 \\ D &= n^2 - k^2 - \sin^2\theta_i \end{aligned} \tag{13}$$

are dependent on a material's refractive index. To understand the connection between the Fresnel reflection coefficients R_s and R_p and the Stokes parameters, it helps to visualize the light/matter interaction. Figure 12 shows Hyde's [18] representation of two cases of polarized light incident on a smooth medium of refractive index $\eta = n - \mathrm{j}k$ where $\boldsymbol{E}$, $\boldsymbol{H}$, and $\boldsymbol{k}$ correspond to the wave's electric field, magnetic field, and propagation direction vectors respectively, and the superscripts i, r, and t correspond the to the incident, reflected, and transmitted portions of the wave. The specular plane in Fig. 12 (and in general) is defined as the plane containing the material's surface normal and the incident and reflected light's propagation direction vectors. If the entire electric field vector lies perpendicular to the

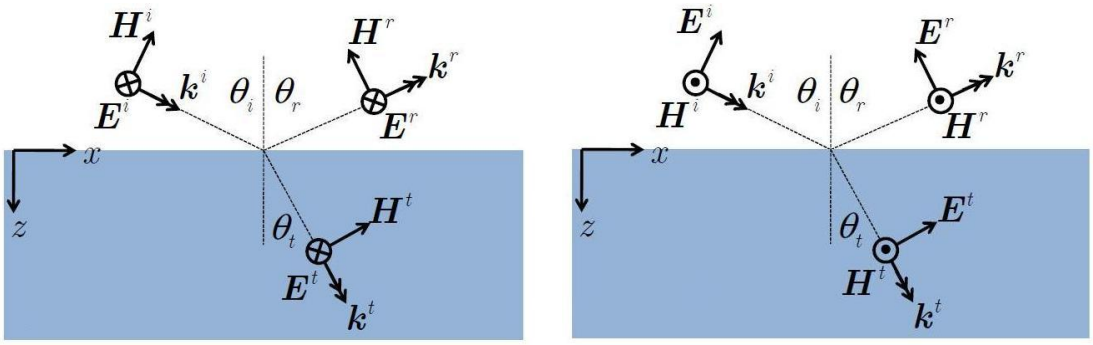

(a) S-Pol **(b) P-Pol**

Figure 12: S-Pol and P-Pol Scattering Geometries [18]

specular plane as in Fig. 12a, the incident light is referred to as perpendicular polarization or S-Pol. If the entire electric field vector is in the specular plane as in Fig. 12b, the incident light is referred to as parallel polarization or P-Pol [18]. Derivations in Torrance [46] and He [15] give the sought after physical model relating the Fresnel reflectance equations to the Stokes parameters as applied to the case of specular reflection from a smooth surface:

$$DOP = \frac{R_s - R_p}{R_s + R_p} \tag{14}$$

2.3.5 Bidirectional Reflectance Distribution Function.

The previous section applied to the case of reflection off a smooth surface. A surface looks smooth to incident light if the surface roughness is much smaller than the light's wavelength. In the visible band, 400 − 700nm, most surfaces look "rough" so the model stated above must be reconsidered. Figure 13 introduces the concept of a Bidirectional Reflectance Distribution Function (BRDF). Instead of modeling reflection as purely specular as with the image on the far left, a BRDF models the reflection of light more realistically; somewhere between specular and diffuse reflection. A BRDF describes, mathematically, how reflected light is directionally distributed within the hemisphere above the material's surface. When constructing a BRDF, whether empirically or analytically, a material surface geometry (smooth/rough/otherwise) must be known or assumed. The

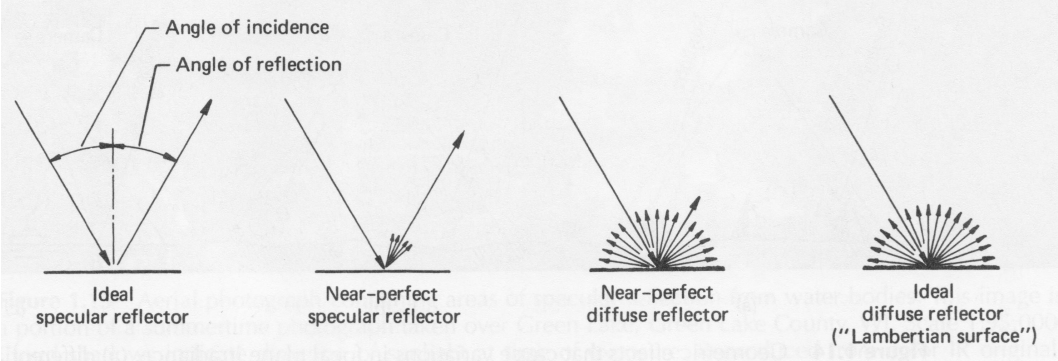

Figure 13: Light Scattering Models [21]

most commonly used model is to think of a surface as a composition of microfacets (similar to the facets of a diamond, but on a much smaller scale), each an ideal specular reflector obeying Snell's law ($\theta_i = \theta_r$) with their own Fresnel reflectivity and their own geometry with respect to the light source and RS receiver [29]. The BRDF surface and viewing geometry used in this work mimics Hyde's [18] and is given in Fig. 14.

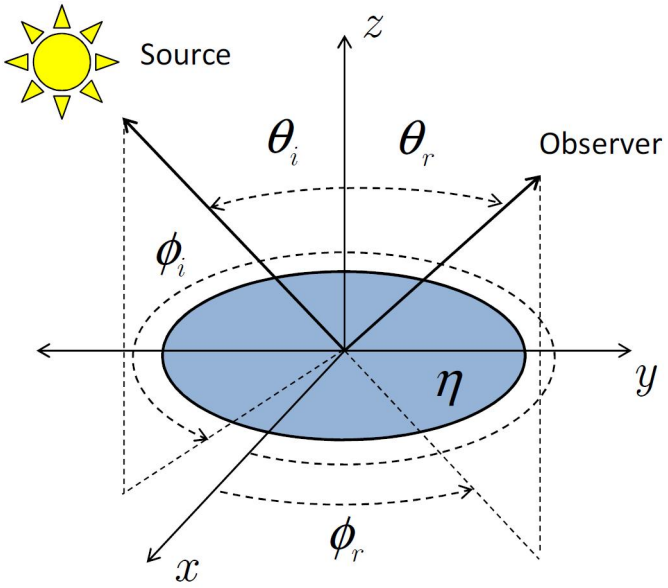

Figure 14: BRDF Surface and Viewing Geometry [18]

The directional distribution of a TEM wave's polarimetric content can equivalently be described by a Polarimetric Bidirectional Reflectance Distribution Function (pBRDF). The pBRDF used in this work is given by

$$f_{jl}(\theta_i, \theta_r, \phi) = \frac{1}{(2\pi)(4\sigma^2)\cos^4\theta} \frac{\exp\left[-\tan^2\theta/(2\sigma^2)\right]}{\cos\theta_r \cos\theta_i} m_{jl}(\theta_i, \theta_r, \phi) \tag{15}$$

where f_{jl} is the element in the j^{th} row, l^{th} column of the Mueller matrix pBRDF, m_{jl} is the element in the j^{th} row, l^{th} column of the Mueller matrix for reflection, ϕ is the azimuthal angle, σ is the surface roughness parameter, and θ is the microfacet angle of orientation relative to the mean surface normal given by

$$\theta = \cos^{-1}\left(\frac{\cos\theta_i + \cos\theta_r}{2\cos\beta}\right) \tag{16}$$

where

$$\cos 2\beta = \cos\theta_r \cos\theta_i + \sin\theta_r \sin\theta_i \cos\phi \tag{17}$$

[18,29,42]. Since this work is confined to the specular plane where $\phi = \pi$, θ and β simplify to

$$\theta = (\theta_r - \theta_i)/2 \qquad \beta = (\theta_r + \theta_i)/2 \tag{18}$$

As shown in Hyde [18] and Thilak [42], using the pBRDF equation to represent DOP once again yields Eq. (14). Substituting in R_s and R_p from (13) and simplifying produces the equation underlying all of this work's results:

$$\begin{aligned} P(n,k,\beta) &= \frac{2A\sin^2\beta\cos\beta}{A^2\cos^2\beta + \sin^4\beta + B^2\cos^2\beta} \\ A &= \sqrt{\frac{\sqrt{C}+D}{2}} \qquad B = \sqrt{\frac{\sqrt{C}-D}{2}} \\ C &= 4n^2k^2 + D^2 \\ D &= n^2 - k^2 - \sin^2\beta \end{aligned} \tag{19}$$

where P is the DOP, or in the case of this work, DOLP.

III. Methodology

With the relevant theory and mathematical framework in place, this chapter describes the method used to apply those concepts to the problem statement, thus producing a hypothesis. Experimentation (rather than simulation) was used to test this work's hypothesis, so a description of the experimental instrument, analysis of the instrument's optical and polarimetric performance, and how the instrument was used to collect data is discussed. The goal of this work is not only to classify, but to characterize unknown targets, so the methods used for classification and characterization are then discussed.

3.1 Experimental Implementation

Data was collected using the Multispectral Stokes Imager (MSSI) instrument (Fig. 15) in the Optical Turbulence Estimation, Compensation, and Simulation (OPTECS) laboratory at the Air Force Institute of Technology. A description of the instrument, its performance, and how it was used to collect data follows.

3.1.1 Instrument Description.

The light source (Fig. 16a) is a mounted, collimated, and diffused warm white Light Emitting Diode (LED) attached to a rotating base which allows for modification of the angles of incidence and reflection. An optical filter mount holds the target in place in a rotation stage. Actuation of the rotating source base and the target rotation stage is controlled via a software interface. The light scattered off the target is reflected off a mirror, which sends it down the rest of the optical train. The Atmospheric Turbulence Simulator (ATS) portion of the instrument (Fig. 16b) was not used for this research, but was left in place for future extensions to this and other OPTECS experiments. Following the ATS, the beam is split with one half the light proceeding to a point polarimeter and the other half proceeding through to the Stokes imager (Fig. 16c). The point polarimeter

automatically calculates the Stokes parameters and DOLP (among many other variables) allowing for verification of input Stokes "truth" states and measured DOLP values. The MSSI consists of a rotating linear polarizer, a manual filter wheel with six 10nm bandgap spectral filters ranging in wavelength from 450 – 700nm in 50nm increments, a focusing lens, an aperture to test diffraction limited performance and reduce irradiance as necessary, and finally, the camera. Given the camera's focal plane size of 2560×1920 pixels, a pixel pitch of 2.2μm, and a Field of View (FOV) of 2.125in. (0.053975m), the MSSI demagnifies the target to 10.38 percent of its original size meaning each pixel images roughly 21μm of the target.

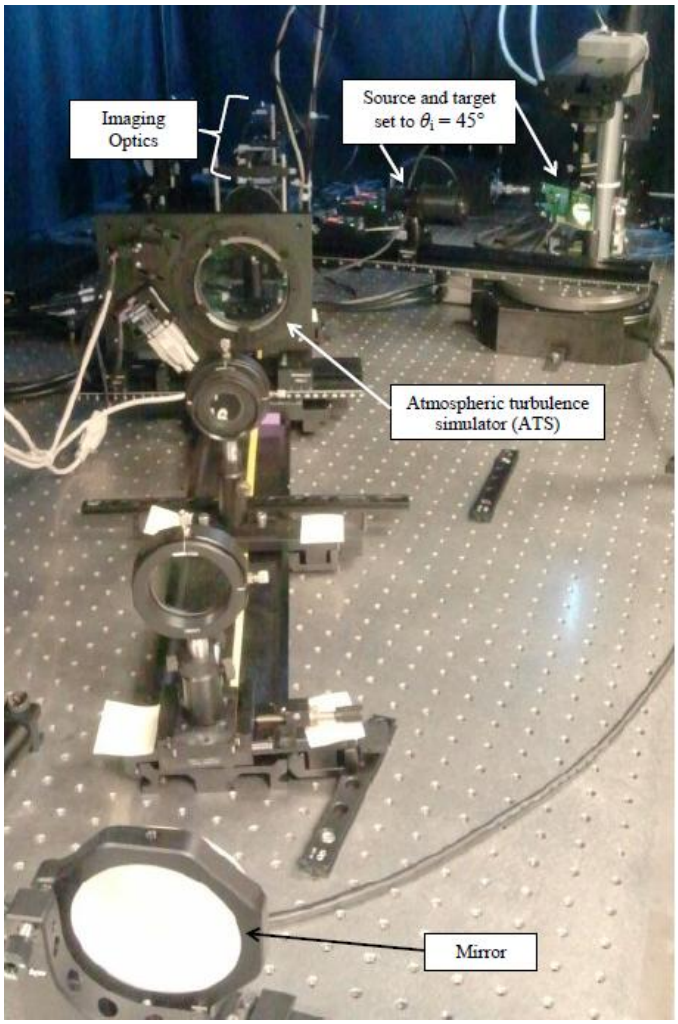

Figure 15: Experimental Instrument

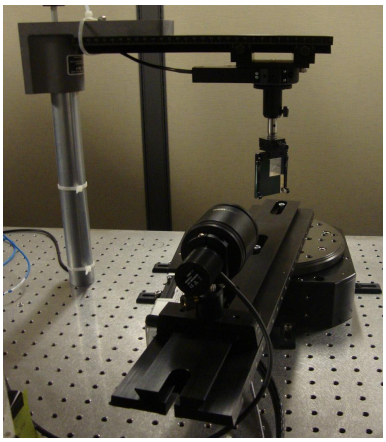

(a) Source and Target

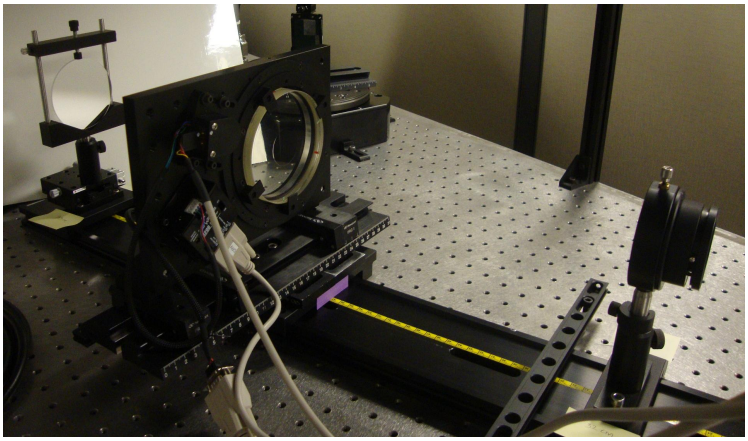

(b) ATS

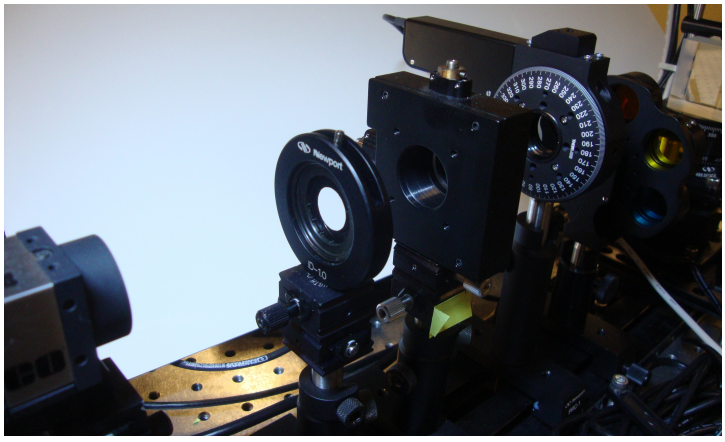

(c) Analyzer and Imaging Optics

Figure 16: Experimental Instrument Components

3.1.2 Instrument Performance.

First, the system's imaging quality as compared to the diffraction limited case is considered, followed by an analysis of the polarimetric response of the system. An imaging system's performance is often expressed by its MTF as compared to an ideal, diffraction limited system. Computation of a system's MTF was discussed in 2.2.4. To measure the MSSI's MTF, a 15μm pinhole was inserted into the target holder and illuminated with a collimated laser beam. The image of this approximated point source is defined as the system's PSF and MATLAB was used to perform the necessary mathematical steps to arrive at the MTF. The MSSI's measured MTF is shown as the dashed blue curve in Fig. 17.

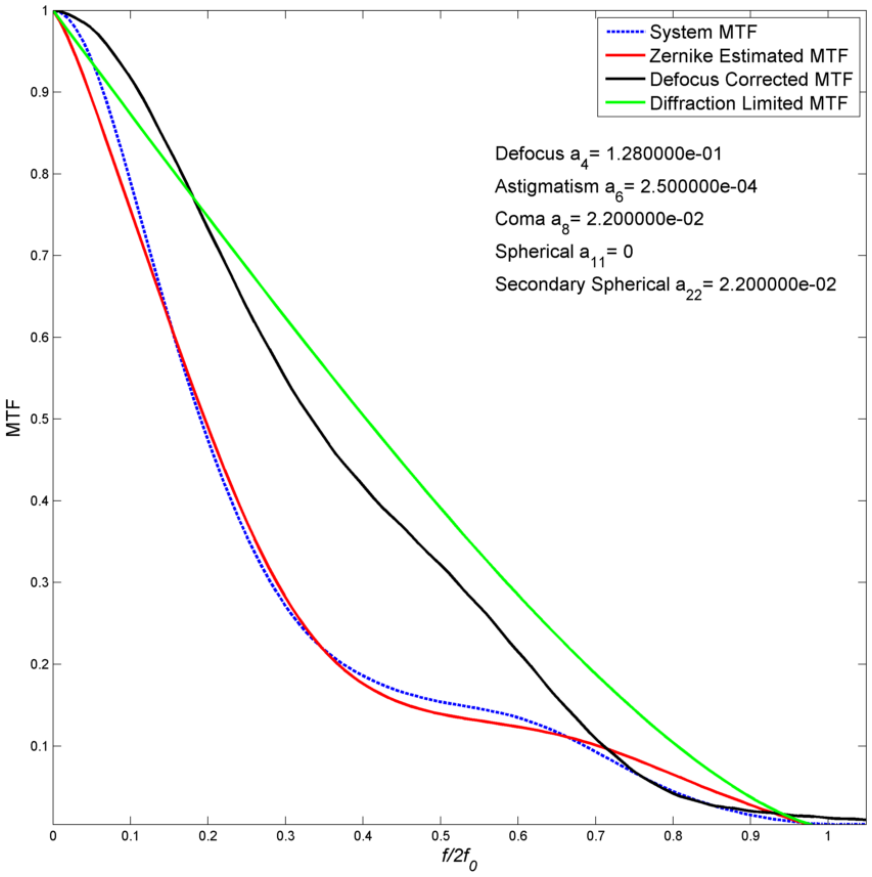

Figure 17: System Defocused, Focused Corrected, and Theoretical MTF Curves

The diffraction limited MTF is shown as the green line in Fig. 17 and was calculated using

$$MTF(f) = \begin{cases} \left| \frac{2}{\pi} \left[\cos^{-1}\left(\frac{f}{2f_0}\right) - \frac{f}{2f_0}\sqrt{1-\left(\frac{f}{2f_0}\right)^2} \right] \right| & \text{if } f \le 2f_0 \\ 0 & \text{otherwise} \end{cases} \tag{20}$$

where $f = \sqrt{f_x^2 + f_y^2}$, $f_x = x/\lambda z_i$, $f_y = y/\lambda z_i$, and f_0 is the system's cutoff frequency defined as $f_0 = d/2\lambda z_i$ [14]. The MTF was found using the laser's wavelength $\lambda = 635$nm, a circular pupil diameter of size $d = 12.3$mm, and an image distance of $z_i = 10.5$cm.

The MTF is a function of spatial frequency f and the closer the system's MTF curve is to the diffraction limited case, the higher the system's spatial frequency resolution will be, signifying a finer resolution imaging capability. Since the MSSI's MTF curve was not diffraction limited, an attempt was made to quantify the aberrations causing the instrument's sub-optimal performance. Potential aberrations were modeled using Zernike polynomials. The plot of the Zernike estimated MTF and the approximated aberration values is shown as the red line in Fig. 17. Clearly the Zernike estimated MTF does not match the system MTF perfectly, but any change to the given polynomial coefficient values caused an increase in mean squared error. Therefore, the given estimation was deemed sufficient. The MSSI's only correctable system aberration is defocus. The change in optical path length necessary to account for the system's defocus was calculated to be -0.14068μm. Measuring to that precision is impractical for this application, so an Air Force resolution bar chart was inserted into the target holder and the system was visually focused. The shape of the camera's pixel intensity histogram distinctly fluctuates as the image reaches and then loses focus. When the shape of the Air Force bar chart's histogram indicated the best possible focus, the pinhole was re-inserted as the target and another PSF measurement was taken revealing marked improvement as shown by the black curve in Fig. 17. The tendency of the MTF to "overshoot" the diffraction limit is termed apodization and is caused by any introduction of absorption into the pupil [14].

With the instrument's imaging quality analyzed, its polarization response was sought. As mentioned in section 2.3.3, a Mueller matrix accounts for the polarization altering effects of components within the optical system. The MSSI's only polarization component is a rotating linear polarizer, which has a known Mueller matrix, given by

$$\boldsymbol{M}_{\mathrm{A}} = \frac{1}{2}\begin{bmatrix} 1 & \cos 2\theta & \sin 2\theta \\ \cos 2\theta & \cos^2 2\theta & \sin 2\theta \cos 2\theta \\ \sin 2\theta & \sin 2\theta \cos 2\theta & \sin^2 2\theta \end{bmatrix} \tag{21}$$

where θ is the angle of the linear polarizer (further referred to as the analyzer) with respect to the x axis. Notice a Mueller matrix is nominally a 4×4 matrix, but since this work does not deal with circular polarization the fourth row and fourth column are unnecessary. If the analyzer was the only element contributing to the system's polarization response, then the input Stokes vector could be found by simply solving

$$\boldsymbol{S}_{\mathrm{out}} = \boldsymbol{M}_{\mathrm{A}} \cdot \boldsymbol{S}_{\mathrm{in}} \tag{22}$$

given a measured output Stokes vector. Unfortunately, passive PI systems are only capable of directly measuring the total irradiance of the field incident upon the polarimeter (given by the first parameter S_0^{out} of the output Stokes vector). The other parameters of the output Stokes vector, S_1^{out} and S_2^{out}, are not measurable making direct inversion of Eq. (22) impossible. Due to this complication another method is sought for finding $\boldsymbol{S}_{\mathrm{in}}$.

A set of "truth" input Stokes vectors was generated by a precision Meadowlark linear polarizer inserted directly after a 633nm LED source (Fig. 18). Using the known input Stokes vectors, a measured set of S_0^{out} parameters, and the data reduction method described below, it was determined that the system's polarization response was not caused by the analyzer alone. Knowing there must be some other component(s) affecting the polarization state, Eq. (22) was updated to include an unknown system Mueller matrix $\boldsymbol{M}_{\mathrm{sys}}$:

$$\boldsymbol{S}_{\mathrm{out}} = \boldsymbol{M}_{\mathrm{A}} \cdot \boldsymbol{M}_{\mathrm{sys}} \cdot \boldsymbol{S}_{\mathrm{in}} \tag{23}$$

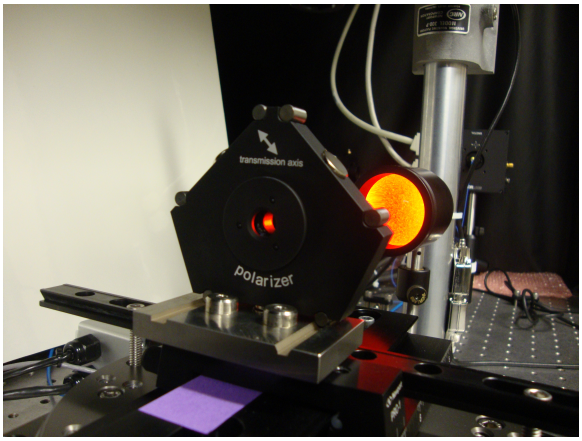

Figure 18: Meadowlark Linear Polarizer and 633nm LED source

Recovering the unknown system Mueller matrix and future unknown input Stokes vectors is possible using the data reduction technique described by Bass [2] and Tyo [47]. The only vector and matrix elements needed from Eq. (23) to express S_0^{out} are

$$S_0^{\text{out}}(\theta) = I(\theta) = \frac{1}{2}\begin{bmatrix}1 & \cos 2\theta & \sin 2\theta\end{bmatrix} \cdot \begin{bmatrix} m_{00} & m_{01} & m_{02} \\ m_{10} & m_{11} & m_{12} \\ m_{20} & m_{21} & m_{22} \end{bmatrix} \cdot \begin{bmatrix} S_0^{\text{in}} \\ S_1^{\text{in}} \\ S_2^{\text{in}} \end{bmatrix} \tag{24}$$

where $\boldsymbol{M}_{\text{sys}}$ is broken down into generic Mueller matrix elements. To demonstrate the simple linear nature of this method, Eq. (24) is multiplied out as

$$\begin{aligned} S_0^{\text{out}}(\theta) = I(\theta) = &\frac{1}{2}[S_0^{\text{in}}(1m_{00} + \cos 2\theta \cdot m_{10} + \sin 2\theta \cdot m_{20}) \\ &+ S_1^{\text{in}}(1m_{01} + \cos 2\theta \cdot m_{11} + \sin 2\theta \cdot m_{21}) \\ &+ S_2^{\text{in}}(1m_{02} + \cos 2\theta \cdot m_{12} + \sin 2\theta \cdot m_{22})] \end{aligned} \tag{25}$$

A system of linear equations can be built up by collecting multiple irradiance S_0^{out} measurements at different analyzer angles θ_j as in

$$\begin{bmatrix} S_0^{\text{out}}(\theta_1) = I(\theta_1) \\ S_0^{\text{out}}(\theta_2) = I(\theta_2) \\ S_0^{\text{out}}(\theta_3) = I(\theta_3) \\ S_0^{\text{out}}(\theta_4) = I(\theta_4) \end{bmatrix} = \frac{1}{2}\begin{bmatrix} 1 & \cos 2\theta_1 & \sin 2\theta_1 \\ 1 & \cos 2\theta_2 & \sin 2\theta_2 \\ 1 & \cos 2\theta_3 & \sin 2\theta_3 \\ 1 & \cos 2\theta_4 & \sin 2\theta_4 \end{bmatrix} \cdot \begin{bmatrix} m_{00} & m_{01} & m_{02} \\ m_{10} & m_{11} & m_{12} \\ m_{20} & m_{21} & m_{22} \end{bmatrix} \cdot \begin{bmatrix} S_0^{\text{in}} \\ S_1^{\text{in}} \\ S_2^{\text{in}} \end{bmatrix} \tag{26}$$

The $S_0^{\text{out}}(\theta_j)$ total irradiance values of Eq. (26) are measured by the camera, the θ_j values of the analyzer Mueller matrix are known, and the input Stokes vector values are known given the truth state generated by the Meadowlark linear polarizer. Knowing these values it is possible to determine all nine $\boldsymbol{M}_{\text{sys}}$ elements with a minimum of nine linear equations. An over-determined system approach was taken in this work. In total, 16 linear equations were produced by collecting 16 irradiance data sets in the form of videos which were later separated into S_0^{out} image frames and averaged over each set of frames. The 16 videos correspond to the following algorithm of data collection:

1. Set up and turn on the warm white diode source
2. Set Meadowlark linear polarizer (input Stokes vector) to horizontal state
3. Rotate analyzer to $\theta_j = 0°, 45°, 90°,$ and $135°$ taking a video at each angle
4. Repeat steps 2 and 3 for remaining input Stokes states (vertical, +45°, and −45°)

The analyzer angles used are arbitrary, but the angles chosen for this work are conventionally used and correspond to the angles used in the fabrication of Kulkarni and Gruev's [19] new division of focal plane multispectral polarimeter, a sensor the MSSI could be adapted to use in the future. MATLAB was used to set up the matrices in Eq. (26) and use of the proper matrix operations yielded the unknown $\boldsymbol{M}_{\text{sys}}$. Following this procedure the calculated $\boldsymbol{M}_{\text{sys}}$ was inserted back into Eq. (23) and the correct "truth" input Stokes vectors were recovered, proving the validity of the calculated $\boldsymbol{M}_{\text{sys}}$. Since polarization response is wavelength dependent, this procedure was repeated for each of the six spectral filters used in this work. The only complication encountered during data acquisition at each wavelength was chromatic aberration, as discussed in section 2.2.2. The presence of chromatic aberration required the system be manually focused after each spectral filter change. With $\boldsymbol{M}_{\text{sys}}$ known for each wavelength, the only remaining experimental task was to collect polarimetric data of targets at multiple wavelengths.

3.1.3 Multispectral Polarimetric Data Collection Algorithm.

The algorithm used to collect target data closely resembles that used to find $\boldsymbol{M}_{\text{sys}}$ for each wavelength and is as follows.

1. Choose target and insert into the target holder
2. Rotate target and source to achieve desired specular angle of incidence
3. Turn on source
4. Rotate analyzer to 90° to allow maximum irradiance through system
5. Rotate filter wheel to spectral filter with highest transmittance
6. Adjust source intensity to ensure no camera pixels are saturated
7. Rotate filter wheel to desired measurement wavelength filter
8. Manually focus system
9. Center target area of interest using software cross hairs and target surface feature
10. Rotate analyzer to $\theta = 0°, 45°, 90°,$ and 135° taking a set of frames at each angle
11. Repeat steps 7 through 10 for each measurement wavelength
12. Repeat steps 2 through 11 for each desired angle of incidence

This manual, iterative process of data collection is time consuming and fraught with misregistration issues (discussed further in subsequent sections), but suffices for the purpose of demonstrating this work's novel data analysis algorithm. Potential steps to automate and improve upon the data collection algorithm are discussed in section 5.2.

3.2 Data Analysis Algorithm

Since the variable of interest to this work, the index of refraction, is different at each wavelength (as evidenced by dispersion), the data analysis algorithm must consist of more than arranging the collected data into a set of linear DOLP equations and attempting to solve for η. In order to create a well-posed set of equations, the non-linear least squares solver used to find η (MATLAB's *lsqcurvefit* function) must be solving for a variable that does not vary with wavelength. Given the theoretical background and the mathematical

framework from Chapter II, a novel hypothesis was formed that the dispersion equations for dielectric and metallic materials could be substituted in place of n and k in the pBRDF-based DOLP equation (Eq. (19)). The non-linear least squares solver could then search for the wavelength-independent dispersion equation constants (A_i for dielectrics and ω_p for metals) that satisfied the empirical DOLP values on the left-hand side of Eq. (19). In order to test this theory, the material must first be classified as dielectric or metallic.

3.2.1 Material Classification.

In his work, Hyde [18] uses a pBRDF model to simulate the DOLP for different materials of differing surface roughness. He notes that the maximum DOLP values achieved for dielectric and metallic materials are approximately 1 and 0.3, respectively. He also mentions that other material classification techniques [4, 45, 52] take advantage of the generalization that dielectric materials strongly polarize scattered light, whereas metallic materials weakly polarize scattered light. This work uses the maximum DOLP values found by Hyde as simple threshold classifiers. In order to use the threshold values to classify each pixel, the DOLP of each pixel must first be found. The frames of irradiance data of a target from the data collection algorithm are averaged and used to find the input Stokes vector of each pixel at each wavelength. The DOLP of each pixel is found for each wavelength using the calculated Stokes parameters as in Eq. (10). Then, the DOLP values of one pixel across all wavelengths are averaged. This one, wavelength averaged DOLP value per pixel determines whether that pixel is classified as a dielectric or a metal. If the averaged DOLP is > 0.3, the pixel is classified as dielectric and if DOLP is ≤ 0.3, the pixel is classified as metal. Hyde warns, though, that DOLP varies over angle of incidence, so the model should not be construed as a rule, but rather a guide. At near-normal incident angles a better classification technique may be to use the derivative of the DOLP values over wavelength due to the tendency of all materials to polarize scattered light very weakly in that regime. The derivative would be near zero for metals and measurable for dielectrics.

3.2.2 *Material Characterization.*

This work's data analysis code has two non-linear least squares solving routines, one for dielectrics that substitutes the Cauchy dispersion equation into the n variable of Eq. (19), and one for metals that substitutes the Drude dispersion equation into n and k of Eq. (19). Once a pixel is classified, the measured DOLP values of that pixel for each wavelength are sent to the appropriate least squares solver routine and the Cauchy coefficients or the plasma frequency is found. The solver returns the Cauchy coefficients or the plasma frequency which are then plugged back into the appropriate dispersion equation to recover n and k. The entire classification and characterization process is repeated for each pixel and is depicted by Fig. 19. The non-linear least squares solving routines both use MATLAB's *lsqcurvefit* function to find the dispersion equation constants. Reasonable bounds were placed on the potential constant values of between 0 and 5 for the Cauchy coefficients [28] and 1×10^{14} and 1×10^{17} for the plasma frequency [13].

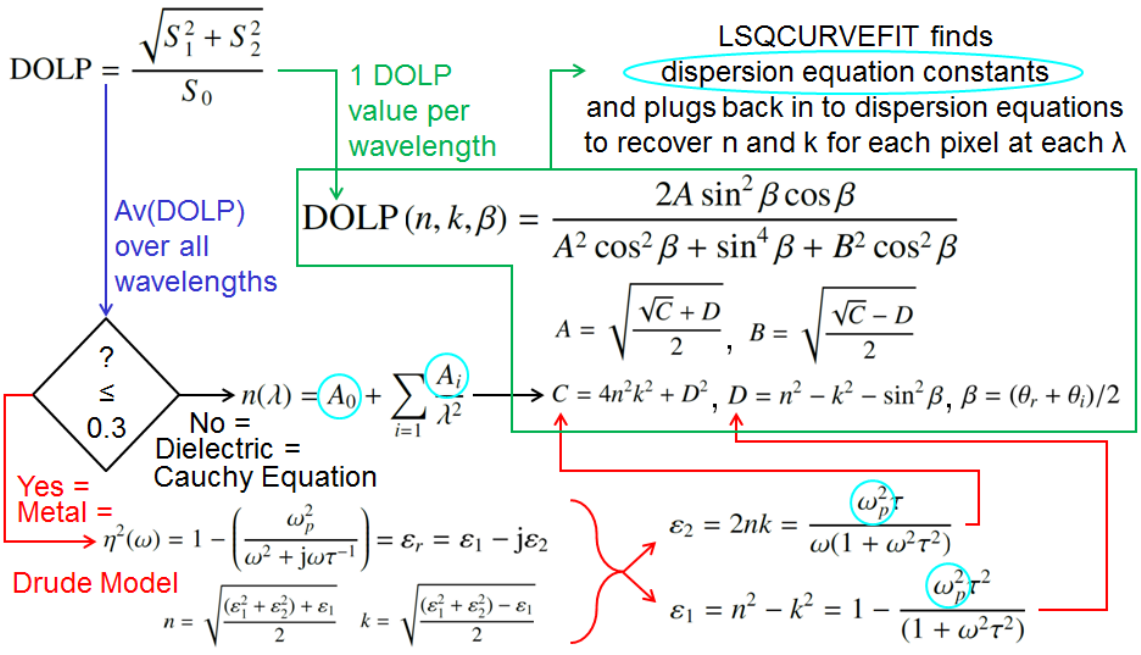

Figure 19: Proposed Per-Pixel MS PI Data Analysis Algorithm Flow Chart

IV. Results and Discussion

As mentioned in section 2.1.2, the benefits of combining MS and PI include their individual conventional abilities to produce true color images and to distinguish between man-made and natural objects, respectively. A set of data products is presented below to demonstrate these benefits. As shown by this work's novel algorithm, another benefit of combining MS and PI is the ability to classify and characterize an unknown target . Figures showing classification and characterization results and tables displaying measured DOLP and refractive index values are given below to show the utility of this work's algorithm.

4.1 Multispectral and Polarimetric Imaging Data Products

Much like the Mueller matrices that accounted for the system's polarization response at each wavelength, a set of multiplication factors was necessary to account for the spectral response of the filters (Fig. 20b shows one example) and the camera (Fig. 20c). The multiplication factors normalize the contribution of each wavelength to ensure the true color image accurately represents the target and were calculated as the inverse of each filter's transmission percentage multiplied by the camera's quantum efficiency. Accounting for the spectral response of the system is not necessary when calculating the Stokes parameters since those are based on irradiance differences measured at the same wavelength rather than across multiple wavelengths. Furthermore, the DOLP values are calculated using normalized Stokes parameters, so any compensation for spectral response would vanish during the normalization process.

Each wavelength's S_0^{out} image was multiplied by the appropriate factor and then normalized to the highest irradiance value across all wavelengths. The normalized values were then assigned to a Red, Green, and Blue (RGB) image data matrix and with MATLAB's image function the true color images were produced (Fig. 21). MATLAB's

image function takes an $n \times m \times 3$ matrix of RGB values and specifies the true color of each pixel from a color map. The abundance of 650nm light incident on the camera, particularly when combined with the high reflectivity of a metallic target, limited the source's output intensity and caused a general lack of dielectric brightness in the mixed material targets.

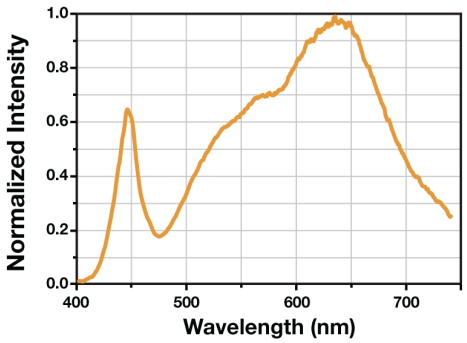

(a) Source Spectrum [44]

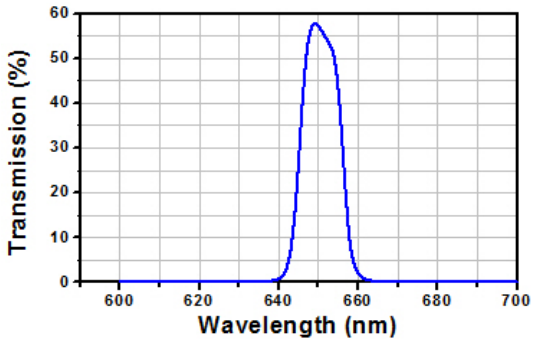

(b) 650nm Spectral Filter Transmission [43]

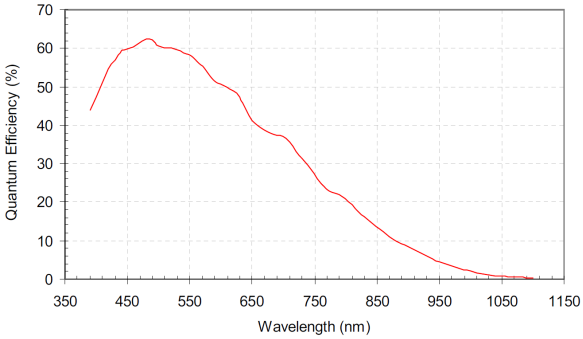

(c) Camera Quantum Efficiency [1]

Figure 20: OPTECS MSSI System Spectral Characteristics

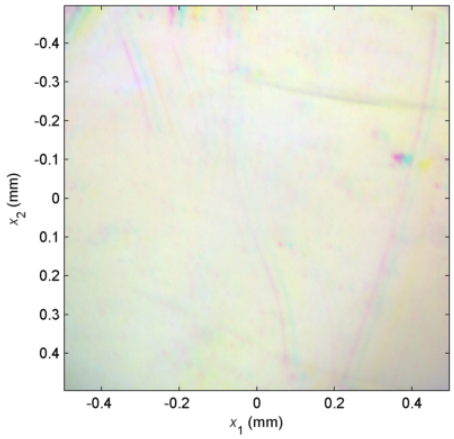

(a) Glass

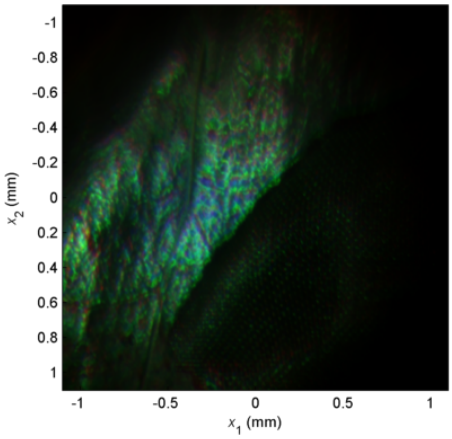

(b) Leaves

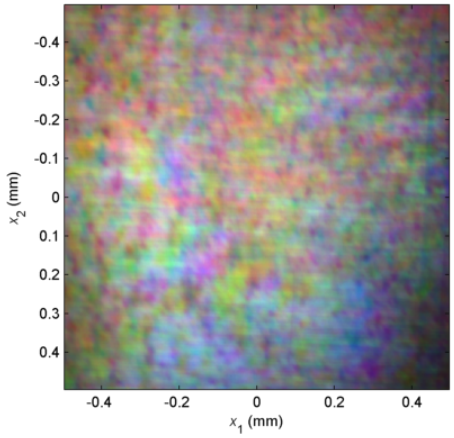

(c) Gold

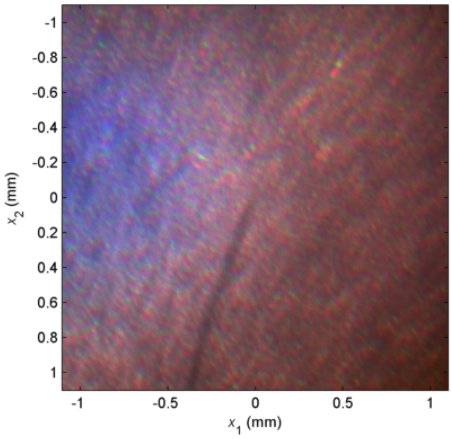

(d) Aluminum

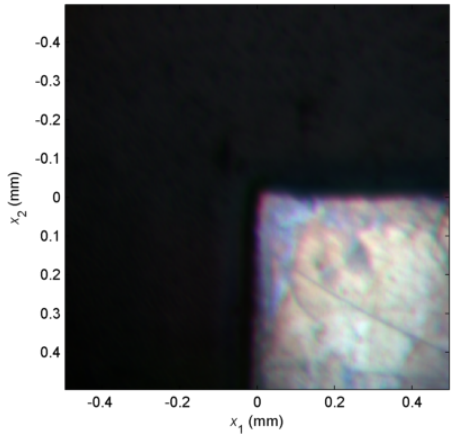

(e) Aluminum and Green Paint

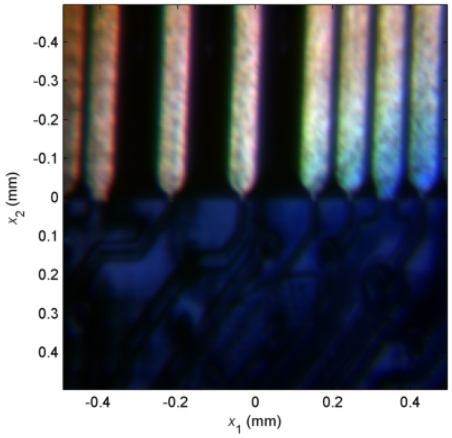

(f) Circuit Board

Figure 21: Experimental Multispectral True Color Images

As expected, glass (Fig. 21a) shows as transparent (interpreted by MATLAB as white, a combination of all colors). Some pixel misregistration can be seen where the magenta, cyan, and yellow spots do not line up to form white. A set of natural and man-made leaves (Fig. 21b) are mainly green with some blue and pink displaying misregistration. A sample of LabSphere InfraGold has hints of its characteristic yellow coloration (Fig. 21c), but misregistration is so abundant in this image that interpretation of the target as gold solely from the true color image is difficult. Data for the rough Aluminum (Al) target shown in Fig. 21d was collected at only 450nm, 550nm, and 650nm. Unfortunately, the approximate wavelengths necessary to construct a true color image align better with 450nm, 550nm, and 700nm (the filters used for all other data collection), so the rough Al target has a misleading orange/pink hue. A target composed of Al with applied green paint clearly shows the Al region and a less distinct green tint to the paint region due to the limitation on source intensity mentioned earlier. The gold fingers and epoxy solder mask of the circuit board (Fig. 21f) are identifiable although the color of the solder mask is not consistent with the original target. The apparent blue color of the green solder mask could be due to the imprecise nature of manually focusing the instrument or lack of camera dynamic range.

4.2 Classification Results

Figure 22 shows the classification result for each target, with DOLP > 0.3 = dielectric and DOLP ≤ 0.3 = metal. The only surprising result was that of the set of leaves (Fig. 22b). The classification is correct, but the DOLP values of the natural leaf are much higher than those of the man-made leaf, which is the opposite of the expected result. The issue here lies not in the theory regarding DOLP values for man-made versus natural targets, but in the data collection scenario. For an operational remote sensing system the target would be much further away from the sensor than is possible to duplicate in a lab environment. As a result, when an operational system images a scene it would "see" a canopy of tree leaves which diffusely scatters light rather than seeing only one highly specular reflecting leaf.

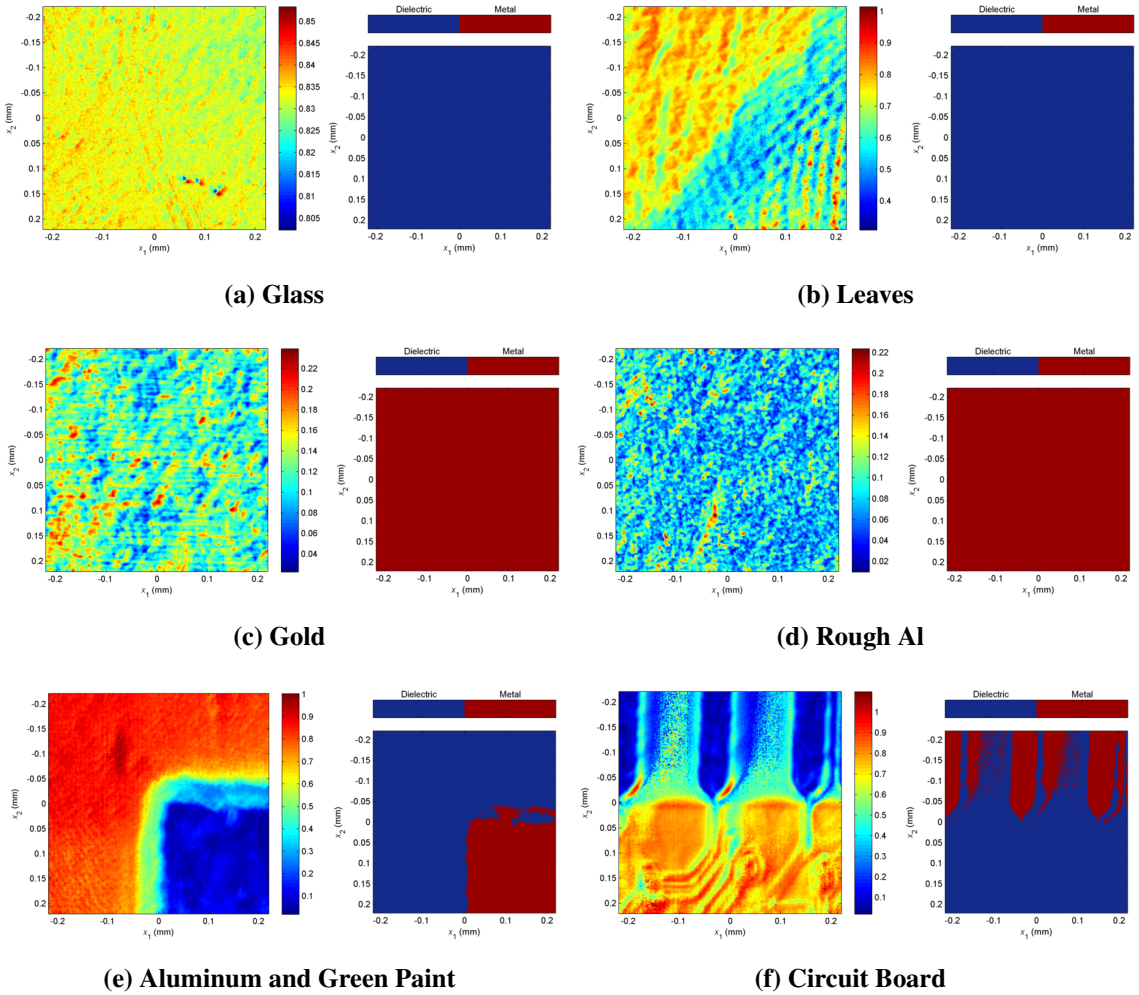

(a) Glass **(b) Leaves**

(c) Gold **(d) Rough Al**

(e) Aluminum and Green Paint **(f) Circuit Board**

Figure 22: Target DOLP Averaged over All Wavelengths (left) and Material Classification Results (right)

Classifying individual pixels of a mixed material target can lead to misclassification as shown by the circuit board and the Al and green paint targets in Fig. 22. Averaging the DOLP over an adjacent grouping of pixels and then classifying could increase the accuracy of the classification. For instance, the small area of misclassified material of the Al and green paint target would be classified correctly if averaged with the surrounding (lower) DOLP values. It may be undesirable to average over many pixels depending on the system's resolution, but in this case, with one pixel imaging only 21μm of the target, the loss of a bit of resolution for more accurate classification would be an acceptable trade-off.

Section 1.2 mentions the importance of correct pixel registration between irradiance images over all wavelengths to this work. One drawback to the manual nature of the MSSI is pixel misregistration. Throughout the data collection process an obvious feature on the target surface was chosen and the cross hairs of the camera software were used to re-center the target's area of interest (typically 200×200 pixels) on that feature. Any misalignment suffered between wavelength measurements is visible in the normalized S_0 images of each target (two examples are shown in Fig. 23). The misalignment in the case of the leaves target is easy to see when examining the center (550 nm) image as opposed to the outer images. The consequence of this misalignment is reduction in classification and characterization accuracy. When the DOLP values of a pixel from each wavelength are passed to the classification algorithm they are averaged. If one value is inflated due to misregistration it could cause misclassification of the pixel. Similarly, with respect to the non-linear least squares solver, the DOLP values used to determine the constants in the dispersion equations would not represent an optimal curve fit scenario if one or more of them was abnormal, thus potentially causing mischaracterization of that pixel.

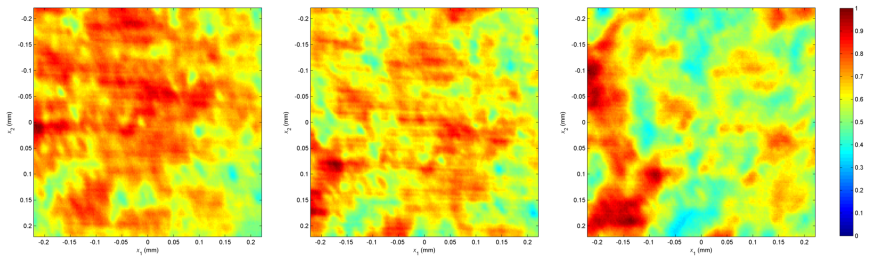

(a) Gold

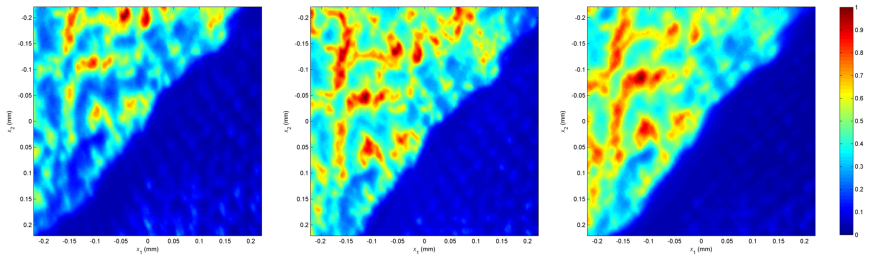

(b) Leaves

Figure 23: Normalized S_0 Parameter Showing 700nm (left), 550nm (center), and 450nm (right) Content of Gold and Leaves

4.3 Characterization Results

As mentioned in section 3.2.2, once a pixel is classified its set of DOLP values (one for each measurement wavelength) is sent to the Cauchy or Drude model function as appropriate. The metallic plasma frequency or set of dielectric Cauchy coefficients is found via non-linear least squares fit to the DOLP values. Then the coefficients or plasma frequency are substituted into the appropriate dispersion equation to recover n and k. Below are the characterization results and analysis for each target examined by this work.

Calculation of a theoretical value for DOLP at each wavelength is possible using Eq. (19) along with the published η values for each target material cited throughout this section and the known angle of incidence. Table 2 gives the results of those calculations as well as the experimentally obtained DOLP values averaged over wavelength. The experimental DOLP values of targets composed of only one material were calculated directly by averaging over every pixel of every wavelength. Mixed material targets were either visually examined to determine an approximate average DOLP value or segmented using a threshold DOLP value and then averaged over each segment. As expected, the dielectric materials exhibit a much higher DOLP than the metallic materials. Also noteworthy is the accuracy of the experimental values despite only defining the "macro" incident angle rather than the more precise angle of incidence that occurs on the micro-facet level. DOLP accuracy is key to the least-squares solver's ability to correctly identify the Cauchy coefficients and plasma frequency per pixel ultimately leading to the correct η.

Table 2: Theoretical and Experimental DOLP Values of each Target, Averaged over λ

	Theoretical		Experimental	
Material	$\theta_i = \theta_r = 45°$	$\theta_i = \theta_r = 60°$	$\theta_i = \theta_r = 45°$	$\theta_i = \theta_r = 60°$
Glass	0.82	0.98	0.83	0.94
Natural Leaf	0.83	0.98	0.77	0.91
Gold	0.17	0.21	0.14	0.14
Aluminum	0.03	0.06	0.07	0.10
Green Paint	0.80	0.94	0.83	0.95
Epoxy	0.83	0.98	0.80	0.90

4.3.1 Dielectric Characterization.

The Cauchy equation, as discussed in section 2.3.2, is a good approximation of dielectric dispersion in the visible band. A limitation of this model, however, is its applicability to only non-lossy dielectrics (non-conductive materials that are transparent in the visible band). Depending on the accuracy desired and the number of MS bands available on a given RS platform, the Sellmeier equation could be used along with a minimum of $2i + 1$ (index value i, not imaginary i) wavelength measurements to recover n and k. This work used the Cauchy equation for dielectric pixels and as a result only recovered n while setting $k = 0$. Figure 24 shows the experimental n values for the glass target and the target consisting of a set of leaves. The mean experimental n value at each wavelength for the glass target is in close agreement with the known n values of BK7 glass (Table 3) computed using the Sellmeier coefficients listed on Schott's N-BK7 datasheet [35].

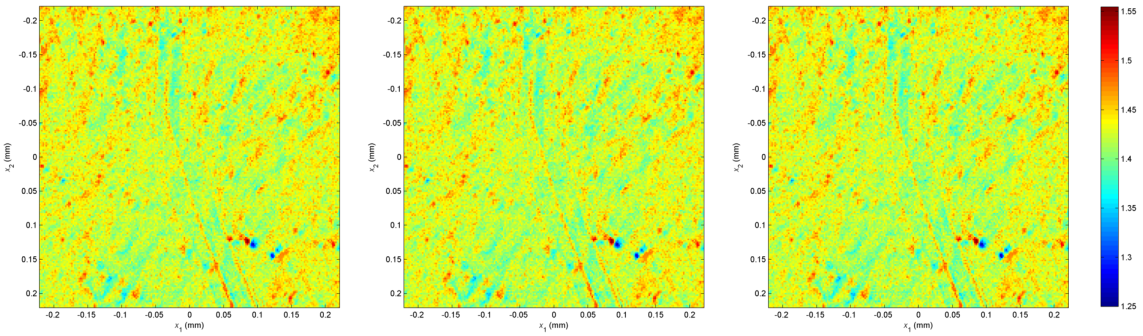

(a) Glass

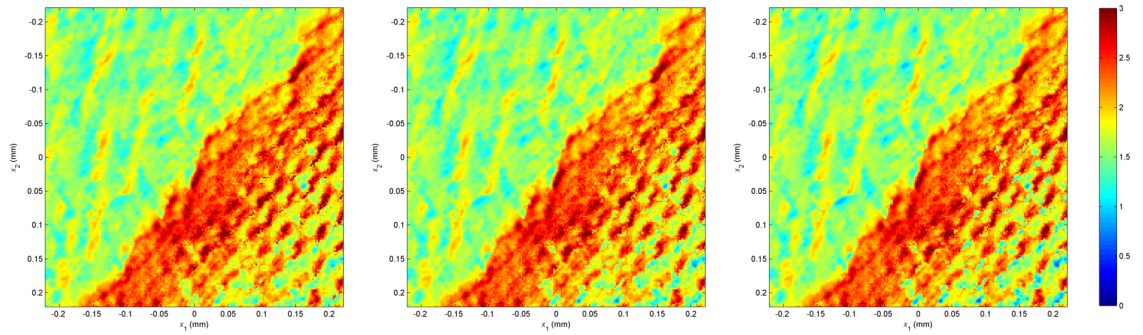

(b) Leaves

Figure 24: Dielectric Target n Values at 450nm (left), 550nm (center), and 700nm (right)

Table 3: Mean, Standard Deviation, and Percent Error of *n* for Glass

λ(nm)	E[n]	σ_n	Known n	% Error
450	1.4267	0.0202	1.52532	6.47
550	1.4260	0.0206	1.51852	6.09
700	1.4255	0.0208	1.51306	5.79

A set of refractive index values is available for natural foliage [48] and is given in Table 4. Judging by the n values indicated by the color scale in Fig. 24, the natural leaf does appear to have a refractive index near 1.5 over each wavelength.

Table 4: Refractive Index of Natural Foliage [48]

λ(nm)	Known n
450	1.527
550	1.509
700	1.493

4.3.2 Metal Characterization.

The usefulness of the Drude model depends on the ability to break η from Eq. (3) into an expression for the real part n and the extinction coefficient k and then substituting those expressions back into Eq. (19). The refractive index is defined as the square root of the complex relative dielectric constant ($\varepsilon_r = \varepsilon_1 - \mathrm{j}\varepsilon_2$) where n and k are related to ε_1 and ε_2 in Palik [28] by

$$n = \sqrt{\frac{(\varepsilon_1^2 + \varepsilon_2^2) + \varepsilon_1}{2}} \quad \text{and} \quad k = \sqrt{\frac{(\varepsilon_1^2 + \varepsilon_2^2) - \varepsilon_1}{2}} \tag{27}$$

and ε_1 and ε_2 are defined in Palik [28] as

$$\varepsilon_1 = n^2 - k^2 = 1 - \frac{\omega_p^2 \tau^2}{(1 + \omega^2 \tau^2)} \quad \text{and} \quad \varepsilon_2 = 2nk = \frac{\omega_p^2 \tau}{\omega(1 + \omega^2 \tau^2)} \tag{28}$$

The electron relaxation rate τ (representing the time between collisions) is dependent on frequency and can be described by

$$\tau = \frac{\omega_p^2}{4\pi\sigma\omega^2} \tag{29}$$

where σ is the material's dc conductivity [28]. In general, τ increases with wavelength and is cited to equal approximately 10^{-14} for most metals [2, 13, 16]. Use of the correct value for τ is very important to accurately calculating η. A good deal of effort was put forth to find consistent published values of τ for gold and aluminum, but with values ranging from 10^{-15} to 10^{-12} (often without a wavelength reference) another method of finding τ was sought. By manually forcing the least-squares solver to use gold's plasma frequency ω_p of 13.6973×10^{15} rad/s [13], it was possible to find values of τ that produced acceptably accurate n and k values for gold ($\tau = 3.25 \times 10^{-14}$, 1.25×10^{-15}, and 4×10^{-15} for 450, 550, and 700nm respectively). The functional form of η used by the least squares solver should ideally not contain any wavelength-dependent variables. For this reason, every instance of τ in Eq. (28) should be replaced by its own functional form (Eq. (29)) and the dc conductivity σ should be treated as another constant for the least squares solver to find.

Table 5 and Fig. 25 show the characterization results of the gold target with $\theta_i = \theta_r = 45^\circ$ and known n and k values from Palik [28]. The results shown for gold use the τ values generated by forcing the plasma frequency to equal its known value. When the raw data was evaluated for presentation the bounds on ω_p were relaxed leaving the solver to work as intended. Allowing the solver to determine ω_p (rather than forcing the known ω_p) produced a mean plasma frequency of 9.62×10^{15} rad/s representing an error of 29.7%. Since gold absorbs near 450nm, the n value at that wavelength is especially sensitive to errors in τ, possibly explaining the relatively larger percent error of n at 450nm. Also, it is possible the n value at 450nm reported in Palik is not quite precise itself.

Table 5: Mean, Standard Deviation, and Percent Error of *n* and *k* for the Gold Target

λ(nm)	E[n]	σ_n	Known n	% Error$_n$	E[k]	σ_k	Known k	% Error$_k$
450	0.7423	0.1926	1.5023	50.59	1.7044	0.7016	1.8785	9.27
550	0.3421	0.1005	0.3593	4.79	2.5539	0.9554	2.6913	5.11
700	0.1725	0.0536	0.1611	7.08	3.4094	1.2160	3.9521	13.73

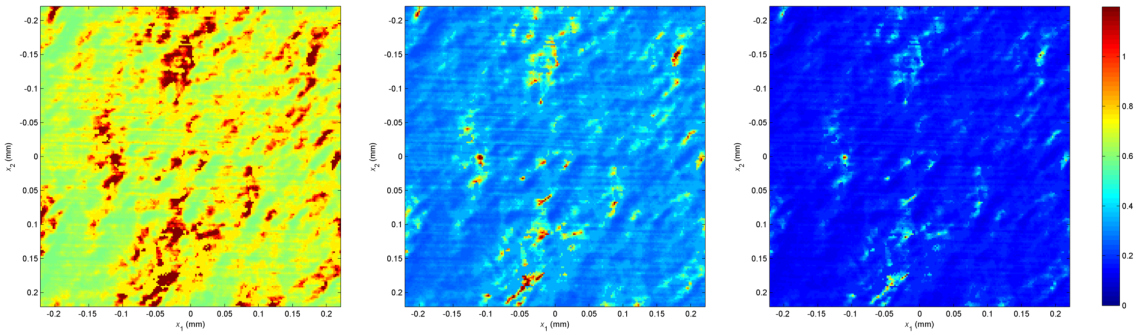

(a) Gold *n*

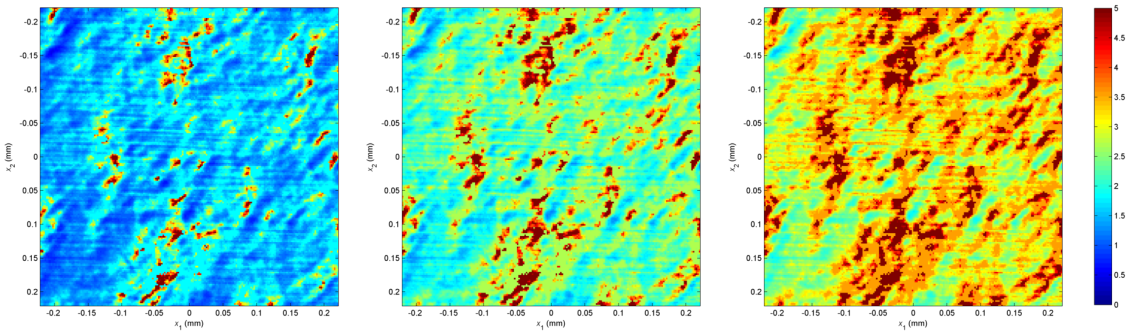

(b) Gold *k*

Figure 25: Experimental Refractive Index Component Values at 450nm (left), 550nm (center), and 700nm (right) for the Gold Target

The τ values used for the gold data were used again when evaluating the rough Al data. Figure 26 shows the resulting n and k images for each wavelength. The mean experimental n and k values given in Table 6 are compared to those given by Palik [28]. The data furnished in Palik were acquired for bulk polished Al, so the errors may be a product of differing surface roughness and the inaccuracy of τ. The mean plasma frequency calculated by the least squares solver was 2.33×10^{-16} rad/s, representing only a 3% error from the known value of 2.4×10^{-16} rad/s [13]. Given a nearly ideal ω_p, the refractive index values likely would also have been nearly ideal had the correct (but unknown) τ values been used.

Table 6: Mean, Standard Deviation, and Percent Error of *n* and *k* for the Rough Al Target

λ(nm)	E[n]	σ_n	Known n	% Error$_n$	E[k]	σ_k	Known k	% Error$_k$
450	1.5412	0.9567	0.6332	132.4	4.4067	3.0504	5.4544	19.2
550	0.7489	0.4775	1.0159	26.28	6.2781	4.2457	6.6273	5.27
650	0.3345	0.2153	1.5580	78.53	7.5875	5.0864	7.7124	1.62

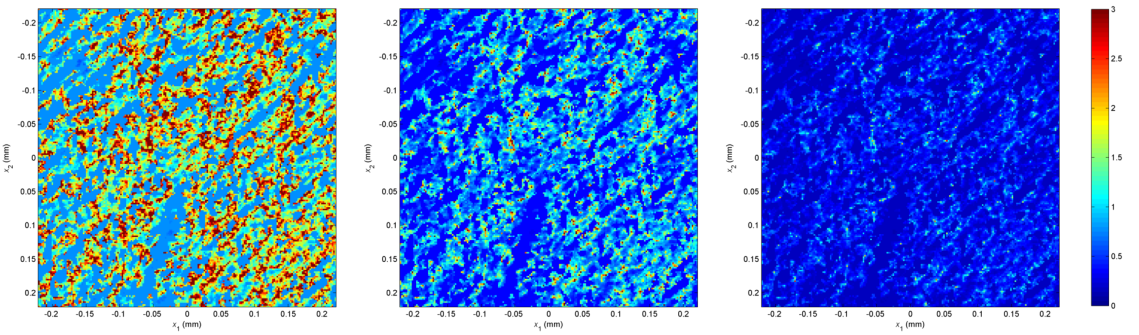

(a) Rough Al *n*

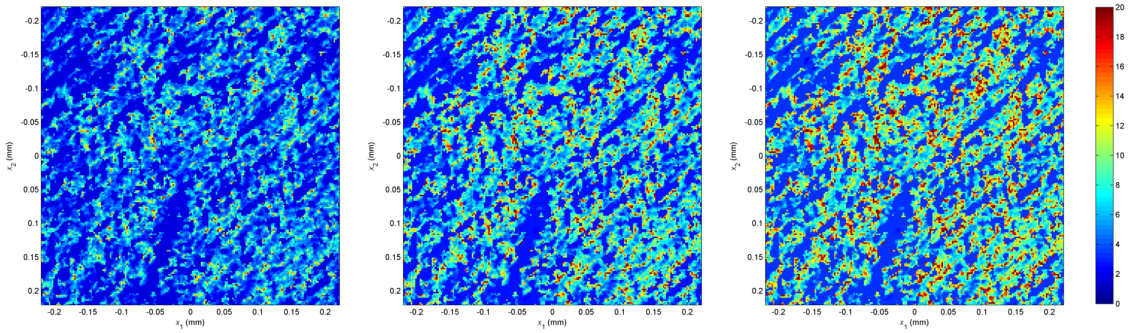

(b) Rough Al *k*

Figure 26: Experimental Refractive Index Component Values at 450nm (left), 550nm (center), and 650nm (right) for the Rough Al Target

4.3.3 Mixed Material Characterization.

The final test of this work's material characterization algorithm was to characterize targets composed of dielectric and metallic materials. Shown and discussed below are the results for the Al with green paint and the circuit board targets.

The Drude model values of τ were originally found for a normally dispersive metal (gold), so it is no surprise that the experimental n values for the Al region in Fig. 27 decrease rather than increase as they should. The decreasing values of n may lead an observer to think the target was copper or gold, but one look at the true color image (if collected at the correct wavelengths) would reveal the metal to be colorless, invalidating the n values. If the least squares solver had been designed to find τ the n values would be more accurate. The green paint region closely matches the n values in Table 7, but due to this work's use of the Cauchy rather than the Sellmeier equation, the k values of green paint were not recovered.

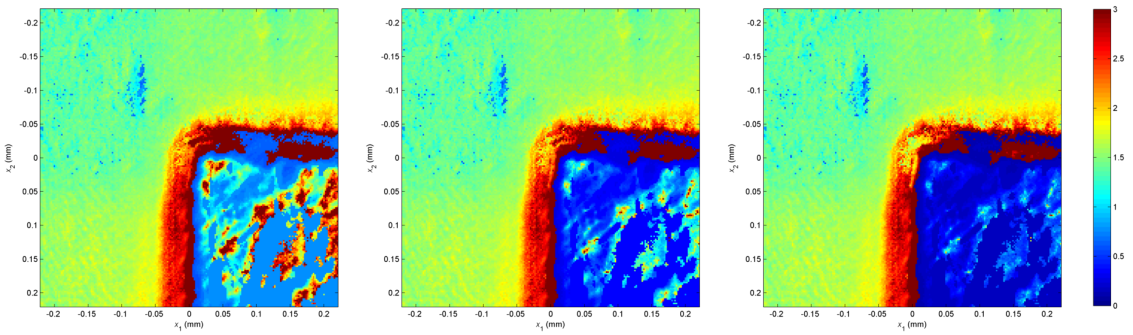

(a) Al with Green Paint *n*

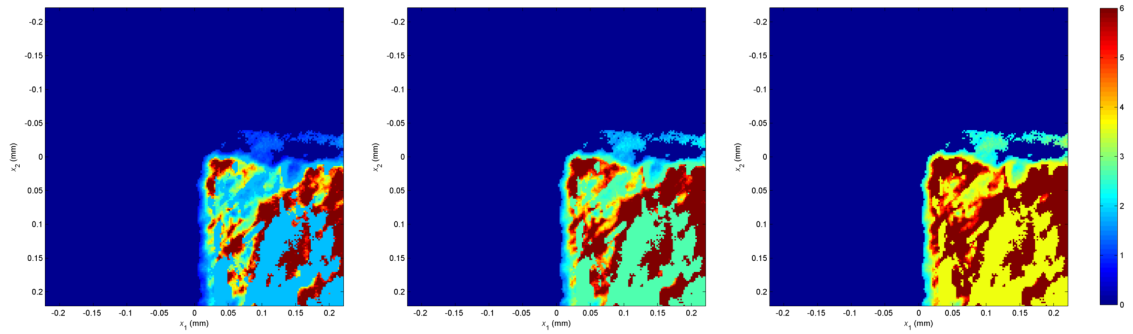

(b) Al with Green Paint *k*

Figure 27: Experimental Refractive Index Component Values at 450nm (left), 550nm (center), and 700nm (right) for the Al with Green Paint Target

Table 7: Known Refractive Index of Green Paint, Extrapolated from Data in Shell [37]

λ(nm)	Extrapolated n	Extrapolated k
450	1.46285	0.296025
550	1.45815	0.298675
700	1.4511	0.30265

Taking a look at the circuit board k value images in Fig. 28b (in which the limits of the data were manipulated only to show better contrast), it is easy to spot the regions that were likely misclassified. The boundaries of the gold fingers are clearly defined and are filled with a high density of large k values. The areas of diffuse pixels were likely misclassified. The misclassification, and corresponding mischaracterization, could be a result of the semi-transparent nature of the epoxy in between the fingers. The cause could be misregistration if at one wavelength the gold fingers overlapped an area of imaged epoxy at another wavelength, but judging from the alignment shown by the normalized S_0 images

in Fig. 29, misregistration is likely not the cause. Another cause of the misclassification could be scattering occurring from a certain depth within the circuit board, essentially displaying the depth of the gold finger, but this is unlikely. Large portions of the k values of the gold at each wavelength agree with the known values for gold given in Table 5. Also, the n values of the gold finger regions decrease with wavelength, suggesting they represent gold or copper. The true color image in Fig. 21f confirms a gold-colored appearance.

The paths of the copper traces leading from the gold regions are fairly visible and have a higher refractive index value than their immediate surroundings. Since the real part of copper's refractive index is a bit lower than gold's in the visible band (1.15-0.2 [28]), there may be a highly insular material protecting the copper traces and the areas in between the gold fingers, producing higher n values in those regions. The n values elsewhere are typical of epoxy used as a solder mask on printed circuit boards [11].

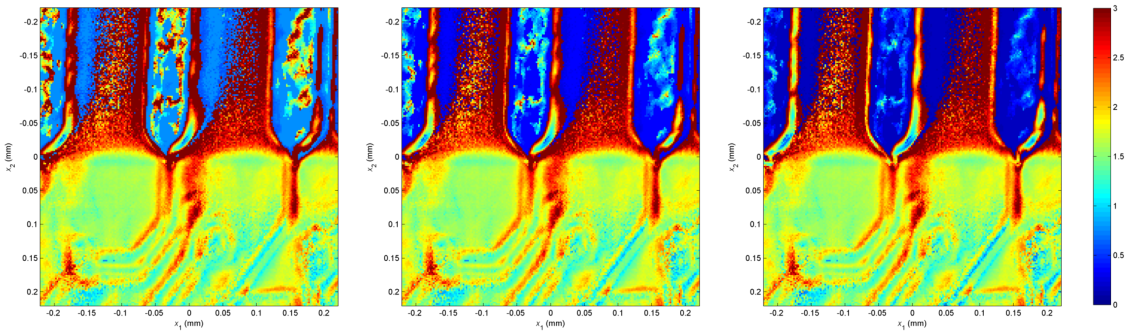

(a) Circuit Board *n*

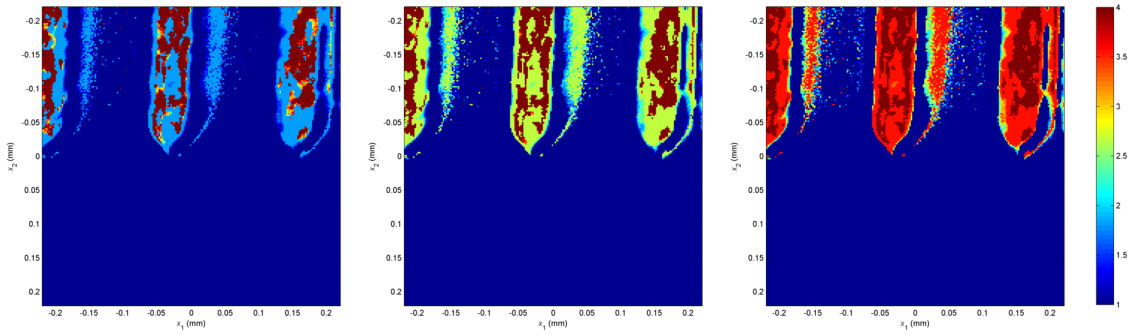

(b) Circuit Board *k*

Figure 28: Experimental Refractive Index Component Values at 450nm (left), 550nm (center), and 700nm (right) for the Circuit Board Target

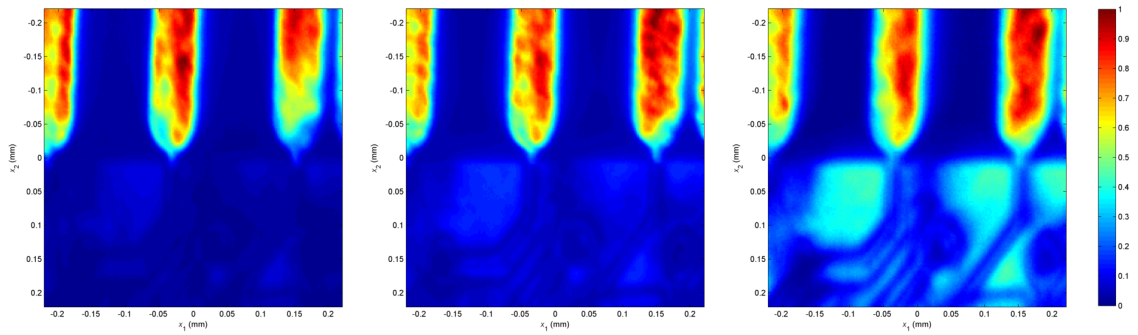

Figure 29: Normalized S_0 Parameter Showing Red (left), Green (center), and Blue (right) Content of Circuit Board

Throughout this chapter, surface irregularities have been apparent in each target's n and k images (edge of where the green paint meets the aluminum, the fabric-like woven texture of the man-made leaf, roughness of the aluminum, etc.). Surface features such as these scatter more light parallel to the surface feature than perpendicular to the feature, increasing the DOLP in those regions and affecting the n and k values.

V. Conclusions and Future Work

5.1 Conclusions

This thesis proved the author's hypothesis correct within acceptable error limits and in a lab environment. With known θ_i and θ_r angles and DOLP measurements collected at multiple wavelengths, the target's index of refraction can be estimated via a non-linear least squares fit using two dispersion equations. Each pixel of an imaged target was classified as dielectric or metallic and was subsequently characterized using a non-linear least squares solver and . A pBRDF-derived equation for the DOLP was given each pixel's set of DOLP values (one for each measurement wavelength) and the least squares solver found the dispersion equation constants that generated the best fit to the experimental data. The dispersion equation constants were substituted back into the dispersion equations yielding the complex index of refraction for each pixel.

Although the characterization results are impressive, the most promising results are displayed in Table 2 comparing the theoretical and experimental DOLP values. As long as the experimental DOLP values are reasonably close to the theoretical values the least squares solver has a good chance of finding dispersion equation constants that produce accurate refractive index values. The modifications to and extensions of this work described in the next section will only serve to increase the algorithm's accuracy.

The combination of multispectral and polarimetric imagery is powerful. The true color images correlated with the refractive index data certainly has the potential to increase target identification accuracy. Even in the absence of polarization content, as is the case for near-normal collection geometries, the true color image alone would provide useful target identification data. While many new remote sensing data interpretation techniques add layers of ever-increasing complexity, this novel algorithm provides elegant simplicity and proven potential to the task of high value target detection and identification.

5.2 Future Work

5.2.1 Material Classification and Characterization Algorithm Improvements.

Rather than using a simple thresholding method to classify each pixel, the technique developed by Wolff [52] may lead to better classification results. Using the Sellmeier in place of the Cauchy dispersion equation to characterize dielectrics would improve the accuracy of the characterization algorithm as it would allow for the recovery of k. Also, as mentioned multiple times, replacing τ in the Drude model dispersion equation and solving for the wavelength-independent dc conductivity would ensure more accurate τ values and likely much more accurate refractive index values.

5.2.2 Expanding Algorithm Region of Validity.

The results presented in this work display the material characterization algorithm's validity at an incident angle of $\theta_i = 45°$. Collection of additional data at many other angles of incidence may prove or disprove the usefulness of this algorithm over a wide range of collection angles. The previously stated limitation of little polarization content at near-normal geometries could be quantified by collecting data as close to the surface normal vector as the instrument allows (approximately $\theta_i = 17°$).

5.2.3 Accounting for Microfacet Geometry.

The AOP can be used to obtain the microfacet normal for each pixel or a certain sized group of pixels. To the author's knowledge a mature and concise technique to accomplish this does not yet exist, but if accomplished could provide a more accurate value of β for the DOLP equation and would allow expansion of this algorithm to out-of-plane scattering. In this work β reduces to simply θ_i due to the condition of specular reflection, but this would not be the case for out-of-plane scattering. The interested reader can find more information regarding AOP techniques and the full β equation in Hyde [18], Robles [33], and Stolz [40].

5.2.4 Incorporation of Atmospheric Turbulence.

Many RS systems such as astronomic telescopes on Earth and imaging systems used from aircraft are affected by atmospheric turbulence. Temperature and pressure differences in the atmosphere cause pockets of air with differing indices of refraction, distorting a RS system's acquired image. The algorithm developed here could be incorporated into the work accomplished by Hyde [18] to create an algorithm capable of producing turbulence-corrected MS polarimetric images.

5.2.5 System Automation.

Future instantiations of the OPTECS Lab MSSI instrument would greatly benefit from automation. The possible misregistration issues mentioned in section 4.2 could be resolved by the use of a calibrated automatic filter wheel and an auto-focusing camera. Automation would also save data collection time, allowing more samples to be tested. Replacing the filter wheel, analyzer, and the camera with a division of focal plane MS polarimeter such as that produced by Kulkarni and Gruev [19] (Fig. 30) would be ideal after better characterization algorithm performance is achieved using the functional form of τ. Using the Gruev polarimeter would also allow for field testing to ensure this algorithm continues to work outside the lab environment.

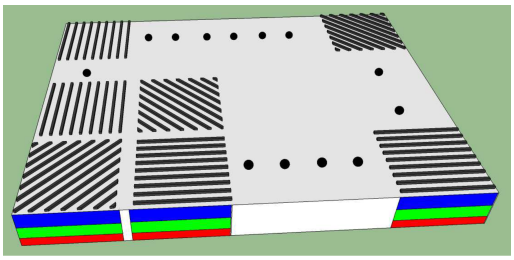

Figure 30: Division of Focal Plane MS Polarimetric Photodetector Array [19]

Bibliography

[1] Aptina Imaging Corporation. "MT9P031 Monochrome addendum", 2008. URL http://www.aptina.com/products/image_sensors/mt9p031i12stm/.

[2] Bass, Michael and Virendra N Mahajan. *Handbook of Optics*, volume 2. McGraw-Hill, 2001.

[3] Buchwald, J.Z. *A Master of Science History: Essays in Honor of Charles Coulston Gillispie*. Springer, 2012.

[4] Chen, Hua and Lawrence B Wolff. "Polarization phase-based method for material classification in computer vision". *International Journal of Computer Vision*, 28(1):73–83, 1998.

[5] Cloude, S. *Polarisation: Applications in Remote Sensing*. Oxford University Press, USA, 2009.

[6] Coffland, Bruce. "Multispectral scanners for wildfire assessment", 2008. URL http://svinetfc4.fs.fed.us/RS2008/b_coffland/index.htm.

[7] Coulson, K.L. *Polarization and Intensity of Light in the Atmosphere*. A. Deepak Pub., 1988.

[8] Curry, Marty. "ER-2 Thematic mapper simulator", 2007. URL http://www.nasa.gov/centers/dryden/research/AirSci/ER-2/tms.html.

[9] Curry, Marty. "ER-2 Sample data and film products", 2008. URL http://www.nasa.gov/centers/dryden/research/AirSci/ER-2/examples.html.

[10] Davidhazy, Andrew. "Spectral rainbow exhibit", 2010. URL http://people.rit.edu/andpph/exhibit-spectrum.html.

[11] Epoxy Technology, Inc. "Understanding optical properties for epoxy applications", 2011. URL http://www.epotek.com/SSCDocs/techtips/Tech%20Tip%2018%20-%20Understanding%20Optical%20Properties%20for%20Epoxy%20Apps.pdf.

[12] Fowles, G.R. *Introduction to Modern Optics*. Dover publications, 1989.

[13] Fox, Mark. *Optical Properties of Solids*. Oxford University Press, New York, 2001.

[14] Goodman, Joseph W. *Introduction to Fourier Optics*, volume 2. McGraw-Hill, New York, 1968.

[15] He, X.D., K.E. Torrance, F.X. Sillion, and D.P. Greenberg. "A comprehensive physical model for light reflection". *SIGGRAPH 1991 Proceedings*, volume 25, 175–186. Computer Graphics, July 1991.

[16] Hecht, E. *Optics*. Addison Wesley, San Francisco, 2002.

[17] Horvath, Mike. "AdditiveColor.svg", 2006. URL http://en.wikipedia.org/wiki/File:AdditiveColor.svg.

[18] Hyde, W. IV, Milo. *Determining the Index of Refraction of an Unknown Object using Passive Polarimetric Imagery Degraded by Atmospheric Turbulence*. Wright-Patterson AFB OH, August 2010. (ADA526413).

[19] Kulkarni, M. and V. Gruev. "Integrated spectral-polarization imaging sensor with aluminum nanowire polarization filters". *Optics Express*, 20(21):22997–23012, 2012.

[20] Labbe, Colleen. "SONAR", 2012. URL http://oceanexplorer.noaa.gov/technology/tools/sonar/sonar.html.

[21] Lillesand, T.M., R.W. Kiefer, J.W. Chipman, et al. *Remote Sensing and Image Interpretation*. (5th Edition). John Wiley & Sons Ltd, 2004.

[22] Matchko, R.M. and G.R. Gerhart. "Polarization measurements using a commercial off-the-shelf digital camera". *Optical Engineering*, 44(2):1–10, 2005.

[23] Merle, Susan. "Volcano O Cone 3", 2012. URL http://oceanexplorer.noaa.gov/explorations/12fire/logs/sept14/media/volcanoo-cone-3.html.

[24] National Oceanic and Atmospheric Administration. "Sonar", Oct 2012. URL http://www.nmfs.noaa.gov/pr/acoustics/sonar.htm.

[25] NOAA Coastal Services Center. "Introduction to Lidar", 2012. URL http://www.csc.noaa.gov/digitalcoast/_/elearning/intro-lidar/player.html.

[26] Olsen, R.C. *Remote Sensing from Air and Space*. SPIE Press, Bellingham, WA, 2007.

[27] Oregon Department of Geology and Mineral Industries. "Oregon Lidar Consortium, DOGAMI Lidar Data Viewer", 2013. URL http://www.oregongeology.org/dogamilidarviewer/.

[28] Palik, Edward D. *Handbook of Optical Constants of Solids*, volume 1. Academic Press, 1985.

[29] Priest, R.G. and S.R. Meier. "Polarimetric microfacet scattering theory with applications to absorptive and reflective surfaces". *Optical Engineering*, 41(5):988–993, May 2002.

[30] Quest Innovations. "Multispectral camera systems", Year not given. URL http://www.quest-innovations.com/multispectral-camera-systems.html.

[31] Richards, M.A., J. Scheer, and W.A. Holm. *Principles of Modern Radar: Basic Principles*. SciTech Publishing, 2010.

[32] Richardson, Annie. "Mount Everest", 1996. URL http://southport.jpl.nasa.gov/cdrom/sirced03/cdrom/DATA/LOCATION/ASIAMIDE/EVEREST/MEVEREST.HTM.

[33] Robles-Kelly, A. and C.P. Huynh. *Imaging Spectroscopy for Scene Analysis*, chapter "Shape and Refractive Index from Polarisation", 241–263. Springer-Verlag, London, 2013.

[34] Roujean, J.L. "A bidirectional reflectance model of the Earth's surface for the correction of remote sensing data". *Journal of Geophysical Research*, 97(D18):20,455–20,468, 1992.

[35] Schott. "N-BK7 data sheet", 2007. URL http://www.us.schott.com/advanced_optics/us/abbe_datasheets/schott_datasheet_n-bk7.pdf?highlighted_text=n-bk7.

[36] Schott, J.R. *Fundamentals of Polarimetric Remote Sensing*. SPIE Press, Bellingham, WA, 2009.

[37] Shell, J.R. *Polarimetric Remote Sensing in the Visible to Near Infrared*. PhD dissertation, Rochester Institute of Technology, Rochester, NY, 2005.

[38] Southeastern Universities Research Association. "Chart of the electromagnetic spectrum", June 2005. URL http://www.sfu.ca/cmns/courses/2011/325/Resources/EM%20Spectrum/sura_electromagnetic_spectrum_small_chart.jpg.

[39] Stokes, G.G. "On the change of refrangibility of light". *Philosophical Transactions of the Royal Society of London*, 142:463–562, 1852.

[40] Stolz, C., M. Ferraton, F. Mériaudeau, et al. "Shape from polarization: a method for solving zenithal angle ambiguity". *Optics Letters*, 37(20), 2012.

[41] Stuart, M. and Fluke Corporation. "Air exfiltration above an exterior window frame", 2011. URL http://homeenergypros.lbl.gov/photo/air-exfiltration-above-an-exterior-window-frame-image-courtesy-of?xg_source=activity.

[42] Thilak, V., D.G. Voelz, and C.D. Creusere. "Polarization-based index of refraction and reflection angle estimation for remote sensing applications". *Applied Optics*, 46(30):7527–7536, 2007.

[43] Thorlabs. "Bandpass filter kits item FB650-10", 2010. URL http://www.thorlabs.com/NewGroupPage9.cfm?ObjectGroup_ID=873.

[44] Thorlabs. "MWWHL3-Warm white mounted high power LED", 2012. URL http://www.thorlabs.com/thorProduct.cfm?partNumber=MWWHL3.

[45] Tominaga, S. and A. Kimachi. "Polarization imaging for material classification". *Optical Engineering*, 47(12):123201, 2008.

[46] Torrance, K.E., E.M. Sparrow, and RC Birkebak. "Polarization, directional distribution, and off-specular peak phenomena in light reflected from roughened surfaces". *JOSA*, 56(7):916–924, 1966.

[47] Tyo, J.S., D.L. Goldstein, D.B. Chenault, and J.A. Shaw. "Review of passive imaging polarimetry for remote sensing applications". *Applied Optics*, 45(22):5453–5469, 2006.

[48] Vanderbilt, V.C. and Lois Grant. "Plant canopy specular reflectance model". *IEEE Transactions on Geoscience and Remote Sensing*, (5):722–730, 1985.

[49] Walraven, R. "Polarization imagery". *Optical Engineering*, 20(1):200114, 1981.

[50] Waltz, E., J. Llinas, et al. *Multisensor Data Fusion*. Artech House, Boston, 1990.

[51] Wolfe, W.L. and G.J. Zissis. *The Infrared Handbook*, volume 1. Office of Naval Research, Department of the Navy, Arlington, VA, 1978.

[52] Wolff, L.B. "Polarization-based material classification from specular reflection". *IEEE Transactions on Pattern Analysis and Machine Intelligence*, 12(11):1059–1071, 1990.

Vita

Melissa A. Sawyer received a B.S. in Electrical Engineering, a B.A. in Business Administration, and a B.A. in Physics from the University of St. Thomas in St. Paul, MN in 2008. As a Lieutenant stationed at Kirtland Air Force Base she took in-residence courses and graduated with a Masters of Business Administration in Policy and Planning from the University of New Mexico in 2011. Following her first Air Force assignment she was assigned to the Air Force Institute of Technology at Wright Patterson Air Force Base in Ohio to earn a Masters in Electrical Engineering, specializing in Electro-Optics. While at AFIT, Melissa served as the chair of AFIT's SPIE Student Chapter membership committee. Her follow-on assignment is with the National Reconnaisance Office.

REPORT DOCUMENTATION PAGE

Form Approved
OMB No. 0704–0188

1. REPORT DATE *(DD–MM–YYYY)*	2. REPORT TYPE	3. DATES COVERED *(From — To)*
21–03–2013	Master's Thesis	Oct 2011–Mar 2013

4. TITLE AND SUBTITLE

Material Characterization using Passive Multispectral Polarimetric Imagery

5a. CONTRACT NUMBER

F1ATA03039J001

5b. GRANT NUMBER

5c. PROGRAM ELEMENT NUMBER

6. AUTHOR(S)

Sawyer, Melissa A., Captain, USAF

5d. PROJECT NUMBER

ENGJON239D

5e. TASK NUMBER

5f. WORK UNIT NUMBER

7. PERFORMING ORGANIZATION NAME(S) AND ADDRESS(ES)

Air Force Institute of Technology
Graduate School of Engineering and Management (AFIT/EN)
2950 Hobson Way
WPAFB, OH 45433-7765

8. PERFORMING ORGANIZATION REPORT NUMBER

AFIT-ENG-13-M-44

9. SPONSORING / MONITORING AGENCY NAME(S) AND ADDRESS(ES)

Air Force Office of Scientific Research
Kent Miller
875 North Randolph St, Suite 325, Room 3112
Arlington, VA 22203
(703) 696-8573, Kent.Miller@afosr.af.mil

10. SPONSOR/MONITOR'S ACRONYM(S)

AFOSR/NE

11. SPONSOR/MONITOR'S REPORT NUMBER(S)

12. DISTRIBUTION / AVAILABILITY STATEMENT

DISTRIBUTION STATEMENT A:
APPROVED FOR PUBLIC RELEASE; DISTRIBUTION UNLIMITED

13. SUPPLEMENTARY NOTES

This work is declared a work of the U.S. Government and is not subject to copyright protection in the United States.

14. ABSTRACT

A new method for characterization of unknown targets using passive multispectral polarimetric imagery is presented. Previous work makes use of a pBRDF derived equation for the degree of linear polarization and with the aid of measurements at multiple incident angles estimates refractive index and reflection angle. This work uses known incident and reflection angles along with dispersion equations and polarimetric data at multiple wavelengths to recover the index of refraction. Although imagery is collected with a division of time polarimeter and a spectral filter wheel in iterative, manual steps, the new algorithm could be applied to any set of registered multispectral polarimetric images most notably those produced by a recently introduced division of focal plane multispectral polarimetric sensor. Experimental results are presented showing the novel algorithm's ability to classify and characterize a range of materials.

15. SUBJECT TERMS

Material characterization; refractive index; polarimetry; multispectral; polarization; polarisation; polarimetric imagery; dispersion; Drude model; Cauchy equation; remote sensing

16. SECURITY CLASSIFICATION OF:			17. LIMITATION OF ABSTRACT	18. NUMBER OF PAGES	19a. NAME OF RESPONSIBLE PERSON
a. REPORT	b. ABSTRACT	c. THIS PAGE			Maj Milo W. Hyde IV (ENG)
U	U	U	UU	74	19b. TELEPHONE NUMBER *(include area code)* (937) 255-3636 x4371 Milo.Hyde@afit.edu